Article

A bioelectrical phase transition patterns the first vertebrate heartbeats

https://doi.org/10.1038/s41586-023-06561-z

Received: 23 December 2022

Accepted: 22 August 2023

Published online: 27 September 2023

Check for updates

Bill Z. Jia[1,2,3], Yitong Qi[1], J. David Wong-Campos[1], Sean G. Megason[2]✉ & Adam E. Cohen[1,4]✉

A regular heartbeat is essential to vertebrate life. In the mature heart, this function is driven by an anatomically localized pacemaker. By contrast, pacemaking capability is broadly distributed in the early embryonic heart[1–3], raising the question of how tissue-scale activity is first established and then maintained during embryonic development. The initial transition of the heart from silent to beating has never been characterized at the timescale of individual electrical events, and the structure in space and time of the early heartbeats remains poorly understood. Using all-optical electrophysiology, we captured the very first heartbeat of a zebrafish and analysed the development of cardiac excitability and conduction around this singular event. The first few beats appeared suddenly, had irregular interbeat intervals, propagated coherently across the primordial heart and emanated from loci that varied between animals and over time. The bioelectrical dynamics were well described by a noisy saddle-node on invariant circle bifurcation with action potential upstroke driven by $Ca_V1.2$. Our work shows how gradual and largely asynchronous development of single-cell bioelectrical properties produces a stereotyped and robust tissue-scale transition from quiescence to coordinated beating.

Cardiac activity during early embryonic development has been documented for more than 2,000 years (refs. 4,5). However, in vivo observations of physiological function in the heart primordium have been limited in spatiotemporal resolution and sample size[6–11]. This scarcity of data means that the bioelectrical mechanisms for the emergence of organized cardiac function are still poorly understood. We asked, how does the heart go from silent to regular beating? What are the intermediate activity states, and how do these states emerge from the ensemble of single-cell developmental trajectories[12]? Here we applied all-optical electrophysiology[13] to observe the first few beats of developing zebrafish hearts and to assess the electrical excitability and connectivity patterns underlying these dynamics.

Capturing the first heartbeat

A first heartbeat is a once-in-a-lifetime event. We sought to capture this event by means of calcium imaging as zebrafish embryos developed from 18–22 hours postfertilization (hpf) (Fig. 1a). During this period, the bilateral cardiac progenitor populations converge and form the heart cone, and early heartbeats have been reported at homologous developmental stages in the chick, rat and mouse[6–11]. At this stage, the progenitors are differentiating into distinct cell types, so we ubiquitously expressed the genetically encoded calcium indicator jGCaMP7f (ref. 14) to capture activity that might be missed by tissue-specific expression. To acquire robust statistics, we combined a system for wide-area all-optical electrophysiology[15] with a custom agarose mould for live imaging of up to 18 embryos concurrently (Fig. 1b, Supplementary File 1, Supplementary Videos 1 and 2 and Methods). This system produced consistent recordings across experiments (Extended Data Fig. 1a). Commonly used tools for arresting cardiac and skeletal muscle motion (*tnnt2a* morpholino and alpha-bungarotoxin messenger RNA (mRNA), respectively) had little effect on the calcium activity (Extended Data Fig. 1b–d). A second red-shifted genetically encoded calcium indicator, FR-GECO1c (ref. 16), also recorded similar dynamics and time of initiation (Extended Data Fig. 1e–g). Dynamics were uncorrelated between neighbouring embryos, implying minimal mechanical or chemical coupling (Extended Data Fig. 1h). These results establish that our experimental preparation faithfully captured the early development of zebrafish cardiac physiology.

Within each embryo, the primordial heart showed an abrupt transition from quiescence to calcium spiking with a stereotyped waveform. These transitions occurred in a tight developmental window of 20.3 ± 0.4 hpf (mean ± s.d., $n = 39$ embryos; Fig. 1c–e and Methods). Calcium dynamics mostly colocalized with fluorescent protein reporters in Tg(*myl7:eGFP*)[17] and Tg(*−36nkx2.5:ZsYellow*)[18] lines, suggesting that the activity occurred in developing cardiomyocytes (Extended Data Fig. 2a–c). Consistent with previous reports, rhythmic calcium dynamics were present before mechanical contractions could be detected (typically 21–22 hpf) using brightfield microscopy (Supplementary Videos 3 and 4)[7,8,11]. We refer to the first large-scale calcium transient as the first heartbeat.

We next asked whether the first heartbeat engaged the whole tissue or was confined to a subset of cells. Before the first heartbeat, we observed occasional single-cell calcium transients, as has been reported

[1]Department of Chemistry and Chemical Biology, Harvard University, Cambridge, MA, USA. [2]Department of Systems Biology, Blavatnik Institute, Harvard Medical School, Boston, MA, USA. [3]Systems, Synthetic and Quantitative Biology PhD Program, Harvard University, Cambridge, MA, USA. [4]Department of Physics, Harvard University, Cambridge, MA, USA. ✉e-mail: megason@hms.harvard.edu; cohen@chemistry.harvard.edu

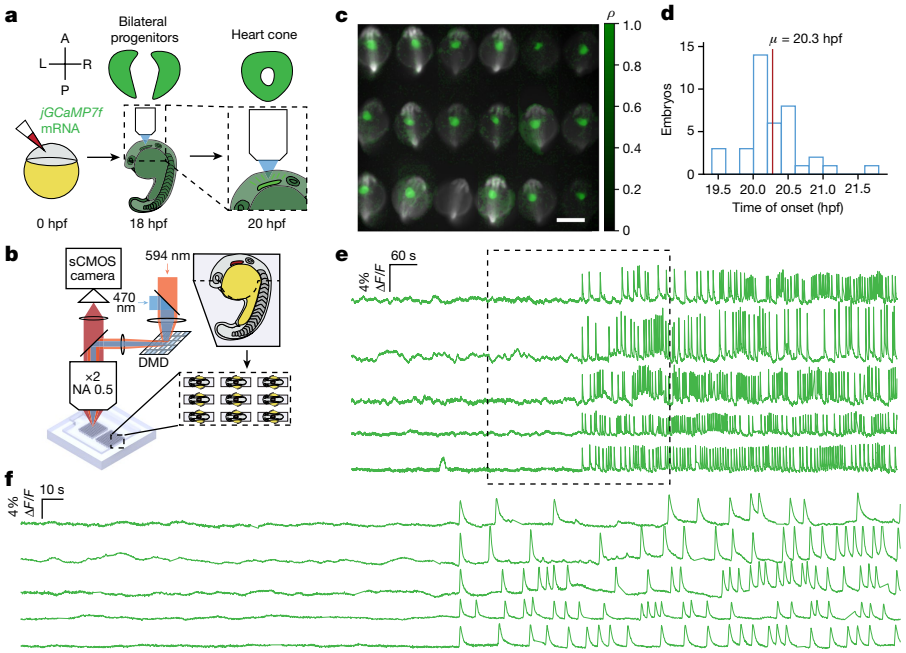

Fig. 1 | Multiplexed time-lapse calcium imaging captures the first heartbeats of zebrafish embryos. a, Injection of mRNA encoding jGCaMP7f for whole-embryo Ca^{2+} imaging during zebrafish heart cone formation. A, anterior; P, posterior; L, left; R, right. **b**, Low-magnification microscopy platform and array mount for multiplexed live imaging and all-optical electrophysiology. DMD, digital micromirror device. **c**, Representative Pearson correlation (green) of individual pixel time traces to putative cardiac activity (three out of three experiments). Activity maps are overlaid on grayscale images of baseline fluorescence. Scale bar, 500 µm. **d**, Histogram of time of onset of the first cardiac calcium spike (n = 39 embryos, three experiments). **e**, jGCaMP7f $\Delta F/F$ measurements of representative hearts aligned by the first calcium spike. **f**, Zoomed-in traces from **e**.

previously[11]. These events were infrequent (0.2–0.7 per minute), long-lived (3.40 ± 2.09 s), lacked a sharp peak and were asynchronous between cells, making them qualitatively distinct from the first heartbeats (Fig. 2a and Extended Data Fig. 3a–d). The first beat usually engaged more than 4,000 µm^2 of tissue, comprising most of the heart primordium, compared to a typical cell size of 82 µm^2 (Extended Data Fig. 3e,f and Supplementary Video 5). However, the first beat occasionally (3 times out of 39) preceded the electrical fusion of the two progenitor fields and only propagated through half of the heart (Fig. 2a and Extended Data Fig. 3g–i). In such cases, the beat engaged the contralateral side within 30 min. During the hour after the first beat, the spatial extent of the spikes and the spatially averaged spike amplitude only increased slightly (area 35 ± 47% increase, amplitude 22 ± 27% increase) and spike width decreased only slightly (−24 ± 10% decrease), (Fig. 2b–d and Extended Data Fig. 3j–o). Therefore, the initiation of the heartbeat was a step change from sparse and slow single-cell transients to sharp, tissue-scale spikes that remained relatively stable in spatial extent and waveform over the following hour of development.

Dynamics of the early heartbeat

We then investigated how the heartbeat became periodic. The first few beats were infrequent and irregularly spaced in time. The interspike interval (ISI) became shorter and more uniform as the heart developed (Fig. 2e). The heart rate increased from 7.1 ± 3.3 beats per minute (bpm) at 10 min postonset (mpo) to 29.6 ± 7.9 bpm at 120 mpo (Fig. 2f). We quantified the heart rate variability by the coefficient of variation (standard deviation/mean) of the ISI. An ISI coefficient of variation of 1 corresponds to a Poisson process and ISI coefficient of variation of 0 corresponds to perfect periodicity. The ISI coefficient of variation decreased from 0.62 (0.44–0.83) (denoted as 'median (interquartile range (IQR))' throughout the text) at 10 mpo to 0.37 (0.26–0.52) at 120 mpo (Fig. 2g).

Excitable to oscillatory transition

The mean heart rate and ISI coefficient of variation of individual embryos followed stereotyped trajectories when aligned temporally to the first beat, suggesting a characteristic transition underlying the dynamics (Fig. 2f,g). We thus sought to understand the nature of the transition from quiescence to beating. This transition can be described as a codimension-1 bifurcation, that is, a step change in dynamics driven by a continuous change in a control parameter. There are just four classes of codimension-1 bifurcations into an oscillatory state[19]. The class of bifurcation determines an oscillator's qualitative dynamics, including oscillation amplitude, frequency and stability, as well as its response to perturbations. Efforts to classify bifurcations in biological oscillators have yielded important insights into physiological function, for example in the computational properties of neurons[19–21] and the sensing mechanisms of cochlear hair cells[22]. We therefore sought to assign the initiation of the heartbeat to one of these classes.

We compared our experimental results to simulated excitable-to-oscillatory transitions, using the action potential model of Morris and Lecar, which is the simplest model that allows simulation of all four bifurcation types (Supplementary Information and Extended Data Fig. 4a,b)[23]. To capture the beat-rate variability in the system, we added white noise to the drive current. Only the saddle-node on invariant circle (SNIC) bifurcation captured the experimental spike timing statistics (Extended Data Fig. 4c). The other bifurcations also differed qualitatively from the data (Supplementary Information), showing graded oscillation amplitude (supercritical Hopf bifurcation) or bistability between oscillatory and silent states (saddle-node, subcritical Hopf bifurcations). By contrast, the SNIC bifurcation predicted a relatively constant spike amplitude near the bifurcation point, and an absence of bistability between silent and spiking states, both consistent with our data.

All SNIC bifurcation models have similar dynamics near the bifurcation point[24], so we proceeded with the simplest, the quadratic integrate-and-fire (QIF) model[19] (Supplementary Information). The

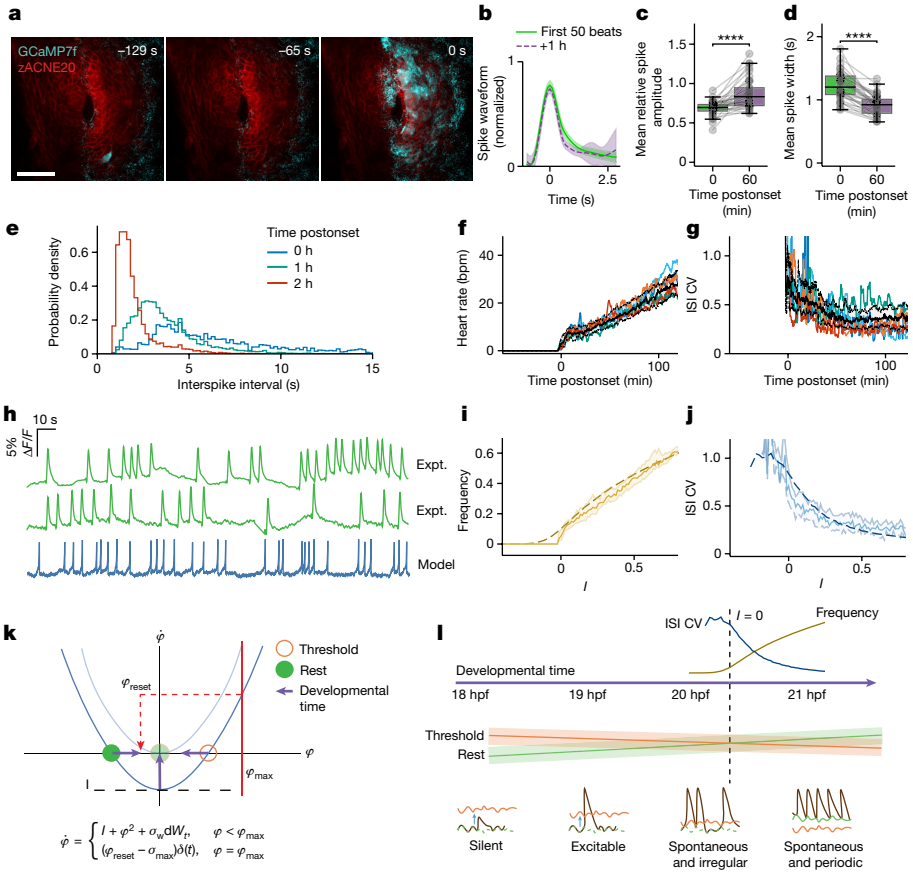

Fig. 2 | The heartbeat starts by means of a noisy tissue-wide SNIC bifurcation. **a**, Single-cell calcium transients followed by a large-scale coherent event at $t = 0$ (three out of three embryos, quantified in Extended Data Fig. 3a–d). Scale bar, 50 µm. **b**, Spike-triggered average waveform over 50 spikes for individual embryos at onset and 1 h postonset. Error bar is standard deviation over spikes at each time sample. **c**,**d**, Average transient amplitude (**c**) and spike width (**d**) over 50 beats starting from the first beat and starting from 1 h later. Circles linked by lines represent successive measurements in the same embryo. Boxplots represent IQR (25th, 50th, 75th percentile) with whiskers representing 1.5× IQR. **e**, Population distribution of ISIs in selected 10-min windows relative to the first heartbeat. **f**,**g**, Beat rate (**f**) and ISI coefficient of variation (ISI CV; **g**) aligned to the first heartbeat. Black line, median; dotted lines and shading, IQR and coloured lines, representative individual traces. **h**, Example traces of the first calcium spikes (Expt., experiment, green; top trace is the middle trace from Fig. 1f, reproduced) and QIF-generated simulation (blue). **i**,**j**, Experimental frequency (**i**) and CV (**j**) jointly fit to the QIF model (dashed line, Supplementary Information, Extended Data Fig. 4) with linear scalings of drive current to developmental time. Shaded region is ±95% CI. **b**–**j**, Same individuals as Fig. 1d, $n = 39$ embryos, three experiments. **k**, Phase portrait of the QIF model as it undergoes a SNIC bifurcation (Supplementary Information). **l**, Schematic describing emergence of spiking regimes in the early heartbeat driven by a noisy phase transition. Shading schematically illustrates noise in rest and threshold values. Statistical tests: **c**, $T = 27.0$, $^{****}P = 4.1 \times 10^{-7}$; **d**, $T = 0.0$, $^{****}P = 5.3 \times 10^{-8}$. Two-sided Wilcoxon signed-rank test.

noisy QIF model comprises just a 'spiking' variable, φ, and two free parameters, the 'injected current', I, and the noise power, σ_w^2. Intuitively, I determines the distance between a stable resting state and an excitation threshold. When φ crosses the excitation threshold, φ spikes and then returns to the resting state (Extended Data Fig. 4d,e). As I increases, the resting state and excitation threshold get closer until they annihilate each other, yielding the transition from excitable to oscillatory. Within a range of values of σ_w^2, the noisy QIF model captured the evolution of both mean beat frequency and ISI coefficient of variation with just a linear scaling of I to developmental time (Fig. 2h–j and Extended Data Fig. 5a–c). The QIF model also reproduced the probability distributions and temporal autocorrelation functions of the experimental ISIs (Extended Data Fig. 5d–g). In summary, the periodic heartbeat emerges through a phase transition-like SNIC bifurcation, bridged by a regime of noisy spontaneous spiking (Fig. 2k,l).

Calcium-voltage coupling

The SNIC bifurcation suggests that early calcium transients arose by noisy crossing of an excitation threshold, followed by positive feedback amplification. The threshold and positive feedback could come from voltage-dependent ion channels, for example voltage-gated calcium channels (VGCCs), or from voltage-independent intracellular mechanisms, for example calcium-induced calcium release[25,26]. To distinguish these possibilities, we generated a transgenic zebrafish line coexpressing jGCaMP7f and a voltage indicator, Voltron1 (ref. 27), in the heart primordium (Fig. 3a). To improve expression in the heart primordium, we developed a new chimeric promoter (*zACNE20-myl7* (*z20m*); Extended Data Fig. 6). Expression under *z20m* colocalized with *myl7* mRNA and pan-myosin heavy chain antibody (MF-20), markers for myocardium (Extended Data Fig. 6). We used a dual-wavelength imaging system and a red-shifted HaloTag ligand dye to simultaneously capture membrane voltage, V_{mem}, and calcium activity in Tg(*z20m:Voltron1-P2A-jGCaMP7f*) embryos (Fig. 3b–d and Supplementary Video 6).

After the onset of beating, there was a 1:1 relation between spikes in V_{mem} and in calcium. The electrical upstroke preceded the Ca^{2+} upstroke by 97 (76–131) ms (Fig. 3c,e), longer than the difference in sensor kinetics (Voltron1 and jGCaMP7f have half-rise times of 0.44 and 27 ms, respectively). Both voltage and Ca^{2+} propagated through the tissue as coherent waves, with Ca^{2+} lagging V_{mem} in space (Fig. 3d

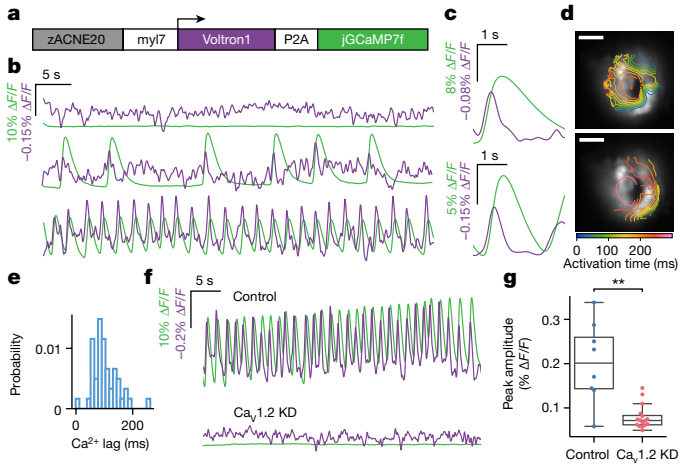

Fig. 3 | The first heartbeats comprise voltage and calcium spikes. a, Genetic construct for simultaneous imaging of calcium and membrane voltage (V_{mem}). **b**, Calcium (green) and V_{mem} (purple) dynamics. The top shows the specimen before onset of calcium dynamics, the middle shows the early heart primordium (6 bpm, estimated 15–30 mpo) and the bottom shows the more mature specimen (25 bpm, estimated 110 mpo). **c**, Spike-triggered averages (STAs) of the bottom two traces in **b**. **d**, Isochronal lines of V_{mem} action potentials corresponding to the 6 and 25 bpm recordings in **b** and **c**. Grayscale image, absolute value of the first spatial principal component (PC) of the calcium recording. Scale bars, 50 µm. **e**, Distribution of lags between voltage and calcium action potential upstrokes (Methods). **a**–**e**, 40 recordings from 36 embryos in one experiment. Data from **f** and **g** are included in analysis. **f**, Dual recordings of V_{mem} and calcium for control and $Ca_V1.2$ knockdown (KD; *cacna1c* morpholino) embryos at 22–23 hpf. **g**, Comparison of amplitude of electrical events in control and knockdown embryos. Boxplot represents IQR (25th, 50th, 75th percentile) with whiskers representing 1.5× IQR. Control, $n = 7$ embryos; KD, $n = 15$ embryos. Statistical test, **g**, $U = 112$, $^{**}P = 2.16 \times 10^{-3}$. Mann–Whitney–Wilcoxon two-sided test.

and Supplementary Video 6), consistent with our previously observed tissue-scale initiation of the heartbeat (Fig. 2a, Extended Data Fig. 3 and Supplementary Video 5). We did not observe any voltage spikes above baseline noise before the onset of Ca^{2+} spiking (Fig. 3b, Extended Data Fig. 1k–o and Methods). Thus, the first few beats comprised electrical action potentials and an accompanying calcium transient.

Because calcium elevation followed voltage depolarization, we probed the role of VGCCs in driving the early dynamics. We performed morpholino knockdown of *cacna1c*, which encodes the pore-forming α 1c subunit of the L-type VGCC $Ca_V1.2$ (ref. 28). In *cacna1c* morphants, neither calcium transients nor electrical action potentials could be detected by 22–23 hpf (Fig. 3f,g and Extended Data Fig. 7a–c). This finding points to $Ca_V1.2$ as the dominant channel for the earliest action potential upstrokes, consistent with pharmacological studies in 36 hpf fish[29] and early mouse hearts[11,30].

We further investigated several other transporters that are important for electrical automaticity in adult pacemaker cardiomyocytes (Extended Data Fig. 7d–h). Morpholino knockdown of the sodium-calcium exchanger *ncx1* slowed the decay of the earliest calcium transients and eventually generated long calcium plateaus, consistent with its role in removing excess calcium from the cytosol. In more mature pacemaker cells, intracellular Ca^{2+} fluctuations are thought to contribute to spontaneous spiking by means of an NCX1-mediated current[30,31]. Knockdown of *ncx1* did not delay the first calcium transients (Extended Data Fig. 7e), suggesting that this mechanism is not yet active in the first heartbeats.

Morpholino knockdown of *hcn4*, which generates the hyperpolarization-activated 'funny current'[32], also did not delay the first few beats and furthermore had no effect on spontaneous calcium dynamics (Extended Data Fig. 7f–h). This observation is consistent with a previous report that the funny current only becomes active between 54 and 102 hpf (ref. 29). Knockdown of *atp1a1a*, a subunit of the Na^+, K^+-ATPase important for regulating resting V_{mem} (ref. 33), delayed initiation and slowed the acceleration of heart rate, consistent with a view that electrical polarization is necessary for the first few beats. Together, these experiments establish depolarization-activated transmembrane Ca^{2+} currents as the driver of the first few beats.

Excitability precedes spontaneity

A key prediction of the SNIC bifurcation model is that it should become increasingly easy to excite action potentials in the time approaching the first spontaneous beats, as the baseline V_{mem} and threshold approach each other (Fig. 2k,l). To test this prediction, we used the channelrhodopsin CoChR[34] to optogenetically depolarize the heart primordium while imaging with FR-GECO1c (Fig. 4a). We applied periodic impulses of blue light targeted to the whole heart and measured the probability of evoking a calcium transient as a function of developmental time (Fig. 4b and Supplementary Video 2). We observed all-or-none responses to individual stimuli, indicative of coherent tissue-wide responses that resembled later spontaneous heartbeats. The heart became optogenetically excitable in a window 90 min before the first spontaneous beats (Fig. 4b–d). Within individual embryos, the response rate to optogenetic stimuli increased from 0% to close to 100% in typically less than 5 min. This rapid transition is qualitatively consistent with the phase transition-like behaviour observed in the endogenous dynamics (Fig. 1e,f and Extended Data Fig. 1f–i). Optogenetic stimulus before spontaneous beating did not affect when the heart subsequently started beating spontaneously or its rate (Extended Data Fig. 1i,j). Optogenetic stimuli did not evoke beats in *cacna1c* morphant fish (Extended Data Fig. 7i,j), consistent with the key role for $Ca_V1.2$ in driving the early action potential.

To understand how the first heartbeats typically engaged the entire heart field (Supplementary Video 5), we investigated the nature of cell coupling before the first few beats. During the epoch in which the heart was excitable but not yet spontaneously active, we targeted optogenetic stimuli to small subregions of the heart in Tg(*z20m:FR GECO1c-P2A-CoChR-eGFP*) fish. These stimuli elicited propagating calcium waves that initiated at the stimulus location (Fig. 4e and Supplementary Video 7). Therefore, cells were coupled before the initiation of the spontaneous heartbeat and could be excited not only by external stimuli but also by their neighbours. Wave propagation speeds were similar between precocious optically evoked waves, 617 (567–767) µm s^{-1}, and early spontaneous activity, 646 (465–772) µm s^{-1} (not significant, Fig. 4f). These speeds were an order of magnitude faster than reported values for calcium waves driven by diffusion of small molecules[35]. Immunofluorescence showed expression of the gap junction protein connexin-43 as early as 18 hpf (Extended Data Fig. 8). These observations combined with our measurements of voltage excitability and action potential propagation (Fig. 3d) suggest that wave propagation was mediated by sharing of V_{mem} between cells, consistent with gap junction coupling. The presence of both electrical excitability and coupling thus primes the heart for a tissue-wide response to the first spontaneous action potential, explaining the sudden transition from silence to large-area coherent heartbeats.

Spatial origins of electrical waves

The capacity for spontaneous activity is widespread in embryonic cardiomyocytes and gradually becomes localized to cells in molecularly distinct pacemaker regions during development[1–3]. Reports on the spatial locus of initiation (LOI) of early heartbeats vary[6–8], and the mechanisms determining its location in the early heart are unknown. To locate the early LOI in zebrafish hearts, we made high-speed (100 Hz) calcium-imaging maps of the spontaneous heartbeats at

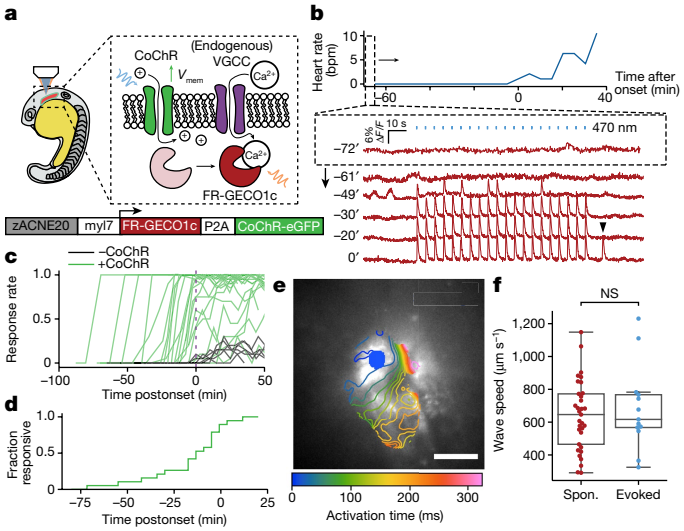

Fig. 4 | The heart primordium is excitable and electrically coupled before the first heartbeat. a, Genetic construct for simultaneous optogenetic stimulation and calcium imaging. **b**, Repeated testing of response to optogenetic stimulation (Methods) in silent hearts. Black triangle indicates the first detected spontaneous beat. **c**, Response rate to optogenetic stimuli in individual embryos. Response rate for embryos not expressing CoChR was a result of spontaneous transients randomly aligning with blue light pulses. **d**, Fraction of the population showing a greater than 50% response rate. **c**,**d**, $n = 5$ embryos −CoChR, $n = 21$ embryos +CoChR, two experiments. **e**, Activation map for triggered averages of calcium elevation evoked by localized stimulus before heartbeat initiation. Scale bar, 50 μm. **f**, Wave propagation speeds for early spontaneous (spon.) activity and activity evoked before first heartbeat. Spontaneous, 90 30-s recordings, $n = 12$ embryos, 3 experiments. Evoked, 13 45-s recordings, $n = 7$ embryos, 2 experiments. Circles represent individual recordings. Boxplot represents IQR (25th, 50th, 75th percentile) with whiskers representing 1.5× IQR. Statistical tests: $t = 0.60$, not significant (NS) $P = 0.55$. Two-tailed unpaired t-test.

20–22 hpf, using the jGCaMP7f reporter (Fig. 5a and Methods). The LOI was variable in location between embryos (Fig. 5b) with a bias for the anterior-left quadrant of the heart cone (38 out of 71 observations across ten embryos). The LOI was typically stable for more than 10 min, but large and sudden displacements of the LOI (greater than 200 μm h^{-1}) between recordings occurred occasionally (mean of one event per 70 min; Extended Data Fig. 2d).

We sought to relate the functional LOI to the underlying pattern of cell identities. The zebrafish heart cone has a well-defined fate map, with distal regions of the cone contributing to the inflow tract, pacemakers and atrium, and proximal regions contributing to the ventricle and outflow tract[36,37]. The early LOI (15–45 mpo) resided primarily in the proximal heart cone and colocalized with *myl7:eGFP* (Extended Data Fig. 2e,f). The LOI drifted outwards as development progressed (15 mpo, 29 (25–31) μm from the inner edge; 105 mpo, 54 (44–65) μm; Fig. 5a–c). Consistent with its anatomical trajectory, the initial LOI expressed *nkx2.5:ZsYellow* more strongly than the later LOI (Fig. 5d).

The proximal Nkx2.5$^+$ location (Extended Data Fig. 2g) of the initial LOI contrasts with the concurrent specification of a reported pacemaker lineage in a distal (roughly 100 μm outwards) and sparse Isl1$^+$/TCF$^+$ population undergoing downregulation of Nkx2.5 (ref. 37). At later stages (roughly 22 hpf), the LOI was located in a region of TCF$^+$ cells (Fig. 5a) with reduced *nkx2.5:ZsYellow* fluorescence (Fig. 5d). There is little cell mixing during zebrafish heart tube formation (Supplementary Video 8, refs. 38,39), confirming that the relative positions of different cell fates are preserved. Consistent with this notion, relative *nkx2.5:ZsYellow* intensity at the original location of the LOI at 15 mpo was unchanged at 105 mpo (Extended Data Fig. 2h). These observations imply that the LOI moved between cell populations. In summary, the location of the early LOI is not precisely specified, but it is preferentially located in the future ventricular myocardium. This location is spatially distinct from the cells that ultimately become pacemakers.

Dynamical determinants of LOI position

The SNIC model predicts that the spontaneous frequency depends strongly on the bifurcation parameter. In a tissue in which there are gradients and spatial variability in developmental trajectories (Fig. 5a–d), one would expect a diversity of spontaneous frequencies. How, then, does the tissue produce coherent beats that emerge from a relatively stable LOI?

We proposed that electrical coupling between cells led to phase locking to the highest frequency oscillator. To test this hypothesis, we used the hyperpolarizing anion channelrhodopsin gtACR2 (ref. 40) and targeted illumination to selectively silence different regions of the heart (Fig. 5e–h and Supplementary Video 9), while simultaneously monitoring calcium with FR-GECO1c. Silencing of the LOI caused a drop in spontaneous frequency, f, and the emergence of a new LOI in a different spot, whereas silencing non-LOI regions caused notably smaller relative frequency drops (f_{after}/f_{before}, LOI silenced, 0.87 (0.66–1.07); non-LOI region silenced, 1.15 (0.96–1.25)) and little LOI displacement (LOI silenced, 70 (47–87) μm; non-LOI region silenced, 25 (15–46) μm: Fig. 5i,j and Supplementary Video 9). These observations indicate the presence of several potential LOIs, with the actual wave origin set by the one with the fastest natural frequency. This mechanism resembles the 'overdrive suppression' that determines the heartbeat initiation site in the adult cardiac conduction system[41]. The presence of overdrive suppression is consistent with previous suggestions based on experiments in dissociated embryonic cardiomyocytes and surgically or genetically perturbed hearts[6,42,43], but to our knowledge has not previously been identified in the intact embryonic heart.

We further tested the overdrive suppression model by focal CoChR pacing of spontaneously active hearts at different frequencies. The optogenetic stimuli only changed beat rate and LOI position when the stimulus frequency was faster than the spontaneous frequency (Extended Data Fig. 9). Furthermore, once pacing stopped, the LOI immediately returned to its previous rhythm and location, with no apparent memory of pacing (Extended Data Fig. 9). The presence of relatively stable LOI locations and an outwards drift punctuated by occasional jumps suggests competition among many cellular oscillators, each with asynchronous maturation towards gradually increasing spontaneous beat rate.

Robustness to electrical heterogeneity

We then asked whether a spatially extended model of an excitable-to-oscillatory transition could account for the above observations on LOI position and response to perturbations. We simulated resistively coupled Morris–Lecar oscillators undergoing a SNIC bifurcation, with a linear spatial gradient of input current, I, to model the observed clustering of the LOI in the anterior-left quadrant. Despite dynamic current noise and static heterogeneity of excitability, the simulations produced coherent waves that emerged from a single LOI and swept the tissue under a broad range of parameters (Supplementary Information and Extended Data Fig. 10). A time-dependent offset in the current recapitulated the beat-rate statistics, as in the single-oscillator QIF model (Extended Data Fig. 10 and Fig. 2f–j). Thus, our model can explain how noisy and gradually changing single-cell excitability properties can produce abrupt and tissue-wide changes in action potential dynamics.

Discussion

Our work provides a coherent picture for how the heart starts beating (Fig. 5k). The heart becomes electrically coupled and excitable

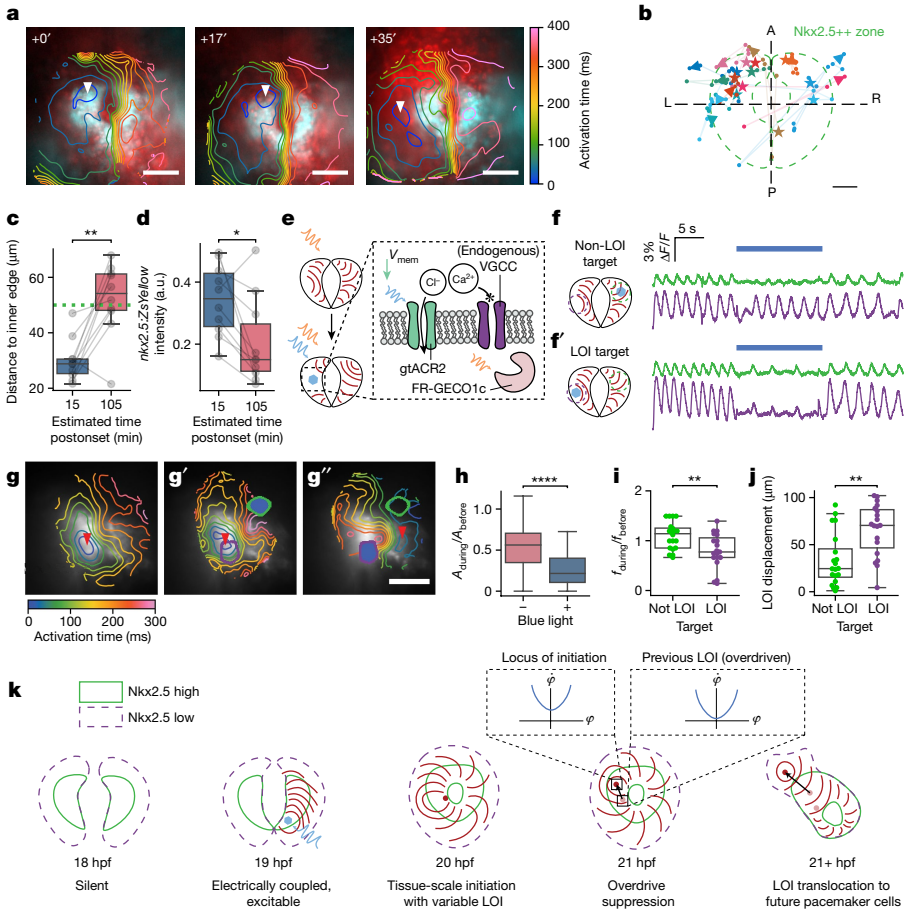

Fig. 5 | Initiation of the early heartbeat is set by competition between spontaneously firing cells. a, Activation maps of spontaneous activity in a representative embryo, showing drift of the LOI (white/red triangle in all panels). Scale bar, 50 µm. Cyan, *nkx2.5:ZsYellow* and red, *TCF:nls-mCherry*. **b**, LOI trajectories for individual embryos. Star indicates initial measurement, arrowhead final measurement. Imaging intervals between 5.5 and 30.5 min (mean 14.6 min). Green dashed line indicates the approximate extent of the (strongly) Nkx2.5^{++} region. Scale bar, 25 µm. **c**, Distance of LOI from Nkx2.5^{++} region inner edge. **d**, *nkx2.5:ZsYellow* intensity at LOI show outwards migration. **b**–**d**, $n = 12$ embryos and three experiments. **e**, Simultaneous optogenetic silencing and calcium imaging. **f**,**f′**, $\Delta F/F$ traces showing localized silencing. Purple, spontaneous LOI and green, non-LOI region. Blue hexagon, optogenetic silencing target. **g**–**g″**, Activation maps of unperturbed activity (**g**) and during targeted silencing at non-LOI (**g′**) and LOI (**g″**). Scale bar, 50 µm. **h**, Relative calcium transient amplitude (A) in the silenced ROI (+, median 0.22 and IQR 0.11–0.40) and distally (−, median 0.56 and IQR 0.35–0.71). **i**,**j**, Relative heart rate (f) (**i**) and LOI displacement (**j**) as a function of optogenetic silencing location. **h**–**j**, 39 observations, 13 embryos and 5 experiments. **k**, Schematic describing early heartbeat spatial patterning. All boxplots represent IQR with whiskers representing 1.5× IQR. Statistical tests: $t = -4.6$, $^{**}P = 1.4 \times 10^{-3}$ (**c**); $W = 5$, $^{*}P = 2.0 \times 10^{-2}$ (**d**); $U = 4{,}350$, $^{****}P = 1.5 \times 10^{-8}$ (**h**); $t = 3.0$, $^{**}P = 5.3 \times 10^{-3}$ (**i**); $U = 300$, $^{**}P = 2.0 \times 10^{-3}$ (**j**). Two-tailed paired t-test (**c**), two-sided Wilcoxon signed-rank test (**d**), Mann–Whitney–Wilcoxon two-sided test (**h**,**j**) and two-tailed unpaired t-test (**i**). a.u., arbitrary unit.

before the first spontaneous beats. Beating begins as the result of a SNIC bifurcation resulting in a sudden transition to full-fledged, $Ca_V1.2$-dependent action potentials that sweep the tissue. Overdrive suppression among many spontaneously active units in the proximal heart cone then assures the presence of one, and only one, LOI in a single beat. The determination of the early LOI is not driven by a molecularly distinct 'pacemaker' cell-type, but rather emerges by biophysical interaction of spatially distributed and noisy oscillators. Isl1$^+$/Nkx2.5$^-$ pacemaker cells only begin to act as the LOI later in development.

The use of advanced optical electrophysiology tools in zebrafish allowed us to characterize this intricate process with high resolution in a minimally invasive way. We observed many features consistent with past studies in amniote embryos, including: asynchronous single-cell calcium transients before the first few beats[11], major functional roles for VGCCs and NCX[11,30], electrical and calcium spikes before mechanical contractions[7,8,11] and variability and lability of the spatial origin of heartbeats[9]. These similarities indicate that many of the early events in heartbeat functional development are conserved across vertebrates. Our results unify these observations and identify how they contribute to the spatiotemporal organization of the earliest cardiac dynamics.

Our data show that the spatial structure of the first heartbeats undergoes a rapid step transition to tissue-scale engagement, but the temporal structure goes through a noisy intermediate between quiescence and periodicity. All biological dynamics are affected by noise, including oscillations[44] and bifurcations[45]. Living systems must overcome this variability to achieve order[46,47], but in many cases noise plays an important role in function[48]. The initiation of the zebrafish heartbeat falls into this latter category. A simple, well-studied model[49] of a stochastic SNIC bifurcation captured all the dynamical steps between quiescence and regular beating.

The function of early self-organized electrical activity is unclear. A rhythmic, spatially structured beat arises well before connection to the circulatory system and blood pumping and is not necessary for survival in early zebrafish embryos[50]. Early activity may contribute to further cardiovascular development, for example, by calcium signalling[51] or mechanical contractility[52,53]. Robust strategies to

initiate physiological function are likely to be broadly important for the progression of embryonic organogenesis.

Online content

Any methods, additional references, Nature Portfolio reporting summaries, source data, extended data, supplementary information, acknowledgements, peer review information; details of author contributions and competing interests; and statements of data and code availability are available at https://doi.org/10.1038/s41586-023-06561-z.

1. DeHaan, R. L. The potassium-sensitivity of isolated embryonic heart cells increases with development. *Dev. Biol.* **23**, 226–240 (1970).
2. Arrenberg, A. B., Stainier, D. Y. R., Baier, H. & Huisken, J. Optogenetic control of cardiac function. *Science* **330**, 971–974 (2010).
3. Bressan, M., Liu, G. & Mikawa, T. Early mesodermal cues assign avian cardiac pacemaker fate potential in a tertiary heart field. *Science* **340**, 744–748 (2013).
4. Falcon, A. & Lefebvre, D. *Aristotle's Generation of Animals: A Critical Guide* (Cambridge Univ. Press, 2018).
5. Sabin, F. Studies on the origin of blood-vessels and of red blood-corpuscles as seen in the living blastoderm of chicks during the second day of incubation. *Contrib. Embryol. Carneg. Inst.* **9**, 214–262 (1920).
6. Patten, B. M. Initiation and early changes in the character of the heart beat in vertebrate embryos. *Physiol. Rev.* **29**, 31–47 (1949).
7. Van Mierop, L. Location of pacemaker in chick embryo heart at the time of initiation of heartbeat. *Am. J. Physiol.* **212**, 407–415 (1967).
8. Kamino, K., Hirota, A. & Fujii, S. Localization of pacemaking activity in early embryonic heart monitored using voltage-sensitive dye. *Nature* **290**, 595–597 (1981).
9. Hirota, A., Kamino, K., Komuro, H., Sakai, T. & Yada, T. Early events in development of electrical activity and contraction in embryonic rat heart assessed by optical recording. *J. Physiol.* **369**, 209–227 (1985).
10. Hirota, A., Kamino, K., Komuro, H. & Sakai, T. Mapping of early development of electrical activity in the embryonic chick heart using multiple-site optical recording. *J. Physiol.* **383**, 711–728 (1987).
11. Tyser, R. C. et al. Calcium handling precedes cardiac differentiation to initiate the first heartbeat. *eLife* **5**, e17113 (2016).
12. Panáková, D., Werdich, A. A. & MacRae, C. A. Wnt11 patterns a myocardial electrical gradient through regulation of the L-type Ca^{2+} channel. *Nature* **466**, 874–878 (2010).
13. Entcheva, E. & Kay, M. W. Cardiac optogenetics: a decade of enlightenment. *Nat. Rev. Cardiol.* **18**, 349–367 (2021).
14. Dana, H. et al. High-performance calcium sensors for imaging activity in neuronal populations and microcompartments. *Nat. Methods* **16**, 649–657 (2019).
15. Werley, C. A., Chien, M.-P. & Cohen, A. E. Ultrawidefield microscope for high-speed fluorescence imaging and targeted optogenetic stimulation. *Biomed. Opt. Express* **8**, 5794–5813 (2017).
16. Dalangin, R. et al. Far-red fluorescent genetically encoded calcium ion indicators. Preprint at *bioRxiv* https://doi.org/10.1101/2020.11.12.380089 (2020).
17. Huang, C.-J., Tu, C.-T., Hsiao, C.-D., Hsieh, F.-J. & Tsai, H.-J. Germ-line transmission of a myocardium-specific GFP transgene reveals critical regulatory elements in the cardiac myosin light chain 2 promoter of zebrafish. *Dev. Dyn.* **228**, 30–40 (2003).
18. Zhou, Y. et al. Latent TGF-β binding protein 3 identifies a second heart field in zebrafish. *Nature* **474**, 645–648 (2011).
19. Izhikevich, E. M. *Dynamical Systems in Neuroscience* (MIT Press, 2007).
20. Hesse, J., Schleimer, J.-H., Maier, N., Schmitz, D. & Schreiber, S. Temperature elevations can induce switches to homoclinic action potentials that alter neural encoding and synchronization. *Nat. Commun.* **13**, 3934 (2022).
21. Meisel, C., Klaus, A., Kuehn, C. & Plenz, D. Critical slowing down governs the transition to neuron spiking. *PLoS Comput. Biol.* **11**, e1004097 (2015).
22. Salvi, J. D., Ó Maoiléidigh, D. & Hudspeth, A. J. Identification of bifurcations from observations of noisy biological oscillators. *Biophys. J.* **111**, 798–812 (2016).
23. Morris, C. & Lecar, H. Voltage oscillations in the barnacle giant muscle fiber. *Biophys. J.* **35**, 193–213 (1981).
24. Kuznetsov, Y. A. *Elements of Applied Bifurcation Theory* Vol. 112 (Springer, 2004).
25. Galione, A. et al. Redundant mechanisms of calcium-induced calcium release underlying calcium waves during fertilization of sea urchin eggs. *Science* **261**, 348–352 (1993).
26. Collier, M. L., Ji, G., Wang, Y.-X. & Kotlikoff, M. I. Calcium-induced calcium release in smooth muscle: loose coupling between the action potential and calcium release. *J. Gen. Physiol.* **115**, 653–662 (2000).
27. Abdelfattah, A. S. et al. Bright and photostable chemigenetic indicators for extended in vivo voltage imaging. *Science* **365**, 699–704 (2019).
28. Rottbauer, W. et al. Growth and function of the embryonic heart depend upon the cardiac-specific L-type calcium channel α1 subunit. *Dev. Cell* **1**, 265–275 (2001).
29. Hou, J. H., Kralj, J. M., Douglass, A. D., Engert, F. & Cohen, A. E. Simultaneous mapping of membrane voltage and calcium in zebrafish heart in vivo reveals chamber-specific developmental transitions in ionic currents. *Front. Physiol.* **5**, 344 (2014).
30. Rapila, R., Korhonen, T. & Tavi, P. Excitation–contraction coupling of the mouse embryonic cardiomyocyte. *J. Gen. Physiol.* **132**, 397–405 (2008).
31. Lakatta, E. G., Maltsev, V. A. & Vinogradova, T. M. A coupled SYSTEM of intracellular Ca^{2+} clocks and surface membrane voltage clocks controls the timekeeping mechanism of the heart's pacemaker. *Circ. Res.* **106**, 659–673 (2010).
32. Jou, C. J. et al. A functional assay for sick sinus syndrome genetic variants. *Cell. Physiol. Biochem.* **42**, 2021–2029 (2017).
33. Shu, X. et al. Na,K-ATPase is essential for embryonic heart development in the zebrafish. *Development* **130**, 6165–6173 (2003).
34. Klapoetke, N. C. et al. Independent optical excitation of distinct neural populations. *Nat. Methods* **11**, 338–346 (2014).
35. Leybaert, L. & Sanderson, M. J. Intercellular Ca^{2+} waves: mechanisms and function. *Physiol. Rev.* **92**, 1359–1392 (2012).
36. Staudt, D. & Stainier, D. Uncovering the molecular and cellular mechanisms of heart development using the zebrafish. *Annu. Rev. Genet.* **46**, 397–418 (2012).
37. Ren, J. et al. Canonical Wnt5b signaling directs outlying Nkx2.5+ mesoderm into pacemaker cardiomyocytes. *Dev. Cell* **50**, 729–743.e5 (2019).
38. Rohr, S., Otten, C. & Abdelilah-Seyfried, S. Asymmetric involution of the myocardial field drives heart tube formation in zebrafish. *Circ. Res.* **102**, e12–e19 (2008).
39. Smith, K. A. et al. Rotation and asymmetric development of the zebrafish heart requires directed migration of cardiac progenitor cells. *Dev. Cell* **14**, 287–297 (2008).
40. Govorunova, E. G., Sineshchekov, O. A., Janz, R., Liu, X. & Spudich, J. L. Natural light-gated anion channels: a family of microbial rhodopsins for advanced optogenetics. *Science* **349**, 647–650 (2015).
41. Vassalle, M. The relationship among cardiac pacemakers. Overdrive suppression. *Circ. Res.* **41**, 269–277 (1977).
42. Cavanaugh, M. W. Pulsation, migration and division in dissociated chick embryo heart cells in vitro. *J. Exp. Zool.* **128**, 573–589 (1955).
43. Chen, J. N. et al. Mutations affecting the cardiovascular system and other internal organs in zebrafish. *Development* **123**, 293–302 (1996).
44. Tsimring, L. S. Noise in biology. *Rep. Prog. Phys.* **77**, 026601 (2014).
45. Dai, L., Vorselen, D., Korolev, K. S. & Gore, J. Generic indicators for loss of resilience before a tipping point leading to population collapse. *Science* **336**, 1175–1177 (2012).
46. Horikawa, K., Ishimatsu, K., Yoshimoto, E., Kondo, S. & Takeda, H. Noise-resistant and synchronized oscillation of the segmentation clock. *Nature* **441**, 719–723 (2006).
47. Tsai, T. Y.-C. et al. An adhesion code ensures robust pattern formation during tissue morphogenesis. *Science* **370**, 113–116 (2020).
48. Hänggi, P. Stochastic resonance in biology: how noise can enhance detection of weak signals and help improve biological information processing. *Chem. Phys. Chem.* **3**, 285–290 (2002).
49. Brunel, N. & Latham, P. E. Firing rate of the noisy quadratic integrate-and-fire neuron. *Neural Comput.* **15**, 2281–2306 (2003).
50. Sehnert, A. J. et al. Cardiac troponin T is essential in sarcomere assembly and cardiac contractility. *Nat. Genet.* **31**, 106–110 (2002).
51. Andersen, N. D. et al. Calcium signaling regulates ventricular hypertrophy during development independent of contraction or blood flow. *J. Mol. Cell. Cardiol.* **80**, 1–9 (2015).
52. Zhu, R. et al. Physical developmental cues for the maturation of human pluripotent stem cell-derived cardiomyocytes. *Stem Cell Res. Ther.* **5**, 117 (2014).
53. North, T. E. et al. Hematopoietic stem cell development is dependent on blood flow. *Cell* **137**, 736–748 (2009).

Methods

Zebrafish strains and maintenance

All vertebrate experiments were approved by the Institutional Animal Care and Use Committee of Harvard University (protocol 10-13-4) or the Harvard Medical Area Standing Committee on Animals (study IS00001263-3). The zebrafish (*Danio rerio*) AB wild-type strain was used for all experiments and generation of transgenic fish. Adult fish were raised at 28.5 °C on a 14 h light/10 h dark cycle. Embryos were collected by crossing female and male adults (3–24 months old). The transgenic lines used in this study are: TgBAC(*−36nkx2.5:zsYellow*)[20], Tg(*7xTCF-Xla.Siam:nlsmCherry*)[54], Tg(*zACNE20:2xLyn-mCherry*) as allele *hm71* (this study), Tg(*zACNE20:FRGECO1c-P2A-CoChR-eGFP*) as allele *hm72* (this study), Tg(*zACNE20-myl7:Voltron1-P2A-jGCaMP7f*) as allele *hm73* (this study) and Tg(*zACNE20-myl7:FRGECO1c-P2A-CoChR-eGFP*) as allele *hm74* (this study). Plasmids used to generate the fish lines by Tol2 transgenesis are deposited at Addgene.

Morpholinos, RNA constructs and microinjection

Morpholinos (Gene Tools) *tnnt2a*-MO (ref. 50) (4 ng), *cacna1c*-MO1 (ref. 51) (2 ng), *cacna1c*-MO2 (ref. 51) (2 ng), atp1a1-MO (ref. 33) (1.5 ng), *ncx1h*-MO (ref. 55) (2 ng) and *hcn4*-MO (ref. 32) (0.2 pmol) were injected at the one-cell stage. The function of each of these morpholinos has been previously validated (Supplementary Table 1). Synthetic mRNAs were transcribed from linearized pMTB plasmid[56] containing insert of interest using the mMessage mMachine SP6 in vitro transcription kit (Thermo Fisher Scientific) and injected at the one-cell stage with 0.1% phenol red (Supplementary Table 2). Morpholino and mRNA sequences are given in Supplementary File 2.

Sample preparation for live functional imaging

Embryos were injected at the one-cell stage with 20 pg mRNA encoding alpha-bungarotoxin, a peptide acetylcholine receptor blocker, to immobilize tail movements[57], 4 ng *tnnt2a* morpholino if performing spatially resolved recordings to eliminate cardiac motion artefacts and the appropriate mRNAs for reporters and channelrhodopsins (Supplementary Table 2). Embryos were raised at 28.5 °C to 16–20 somite stage (17–19 hpf). Egg chorions were removed by immersing embryos in 1 mg ml^{-1} Pronase protease (Sigma) in 0.3× Danieau buffer (17.4 mM NaCl, 0.21 mM KCl, 0.12 mM $MgSO_4$, 0.18 mM $Ca(NO_3)_2$, 1.5 mM HEPES, pH 7.2) for 7 min at room temperature followed by gentle mechanical agitation. A mount was cast in 1.5% agarose in 0.3× Danieau using a custom 'shark-fin' mould (acrylic 'fine detail plastic', Shapeways; designed in Autodesk Inventor 2020; Supplementary File 1) in 35 or 100 mm Petri dishes. Embryos were mounted in 0.3× Danieau and affixed by placing a 0.17 mm glass coverslip over the mount array (×25 imaging) or with a 0.15% low-melt agarose overlay solution (×2 imaging). Figure-wise details of imaging preparations are given in Supplementary Table 2.

Functional imaging with patterned optogenetic stimulus

Live imaging was performed at 28.5 °C or at room temperature using custom optical setups (Fig. 1a)[15,58]. For recordings of jGCaMP7f dynamics, widefield illumination was supplied (0.5–1 mW mm^{-2}) using a 488 nm laser (Coherent Obis) or a 470 nm LED. For spectrally orthogonal stimulation and recording, a 594 nm LED or laser (Cobolt Mambo 100 mW) was used for recording (1–2 mW mm^{-2} when recording at 50 Hz, 0.6 mW mm^{-2} when recording at 10 Hz) and blue light from a 488 nm laser or 470 nm LED (0.5–25 mW mm^{-2}) was patterned by programming a digital micromirror device (ViALUX DLP7000 or Texas Instruments Lightcrafter DLP3000). Imaging was performed through a ×25 numerical aperture (NA) 1.0 objective (Olympus XLPLN25XSVMP2), or ×2 NA 0.5 objective (Olympus MVPLAPO 2XC). Data were recorded on an Orca Flash v.4.0 camera (Hamamatsu) at 10–100 Hz framerate. Temporal control of lasers, digital micromirror device and acquisition was performed using custom MATLAB software through a National Instruments DAQ interface. Image analysis methods are described in the Supplementary Information.

In multiplexed measurements of excitability before initiation of the heartbeat, embryos were mounted at 19–20 somites stage (18.5–19 hpf) as described in the section 'Sample preparation for live functional imaging'. Regions of interest for optogenetic targeting were selected manually using guidance from anatomical features and kept constant during the experiment. Spontaneous activity was recorded for 30 s, and then embryos were subjected to a train of 20 lots of 25 ms blue light pulses at a period of 5 s. Spontaneous activity was then recorded for another 30 s. This was repeated every 5 min.

In gtACR2 targeting experiments, activation maps for spontaneous activity were used to define an LOI target for optogenetic silencing. Several other 'Not LOI' targets for optogenetic silencing were also tested for each embryo. 'Not LOI' targets were defined as those that were above the 50th percentile (47 µm) of distances (across all experiments) from the spontaneous LOI.

Confocal microscopy and morphological analysis

Live imaging was performed at 28.5 °C using a LSM 980 confocal microscope and Zen v.3.2 software (Zeiss). All image stacks were filtered with a 5 × 5 × 1 × 1 (*xyzt*, pixel × pixel × section × frame) median filter to reduce shot noise before further processing. Approximate cell sizes and location of the inner edge of the heart cone were determined by manual tracing of maximum intensity projection images in ImageJ (v.1.53t). Intensity and distance measurements were performed with Python (release v.3.9) scripts using the Scipy stack.

Cellular-resolution imaging of the first heartbeats was performed by scanning a single plane at 3 Hz. Images were filtered with a 5 × 5 × 1 × 1 (*xyzt*, pixel × pixel × section × frame) median filter and twice downsampled in space. Active area was calculated in each frame by summing the number of pixels with intensity greater than 45% of a reference peak value (99.9th percentile of all intensities in the video). To generate videos (Supplementary Video 5), the original recording was filtered with a Gaussian kernel ($(\sigma_x, \sigma_y, \sigma_t)$ = (2 pixel, 2 pixel, 3 frame)) and $\Delta F/F$ was obtained by pixelwise dividing each intensity by the tenth percentile over time.

Simultaneous voltage and calcium imaging

Tg(*zACNE20-myl7:Voltron1-P2A-jGCaMP7f*) embryos were collected and injected with immobilizing agents as described above. Embryos were dechorionated between 6 and 10 hpf using Pronase and incubated overnight in 500 nM JaneliaFluor 608 dye in 0.3× Danieau with 0.5% dimethylsulfoxide (DMSO). At 18 hpf, the embryos were rinsed in 0.3× Danieau, 0.5% DMSO twice for 10 min each, and mounted as described above. Embryos were concurrently illuminated with 488 and 594 nm lasers as described above. Emission light was split using a dichroic mirror and imaged on two sCMOS cameras (Hamamatsu). Registration was performed by imaging a digital micromirror device-projected pattern on both cameras and solving the affine transformation mapping manually defined interest points. Calcium transients were identified by defining a mask based on the first spatial principal component of dynamics in the jGCaMP7f channel and performing spike detection on the average trace as described for other experiments. Candidate matched filter kernels were selected by inspecting the calcium spike-triggered averages traces of Voltron1 fluorescence and used to quantitatively detect voltage spikes (Supplementary Information).

Whole mount immunostaining and in situ hybridization

Immunostaining was performed as described in ref. 59 with some modifications. Briefly, embryos were fixed in 2% paraformaldehyde in PBS at room temperature for 2 h. Embryos were partially de-yolked with forceps before blocking (10% normal goat serum, 1% bovine serum albumin, 0.3% Triton X-100) and application of primary antibodies

(4 °C, overnight). After secondary antibody incubation (4 °C, overnight), embryos were incubated in 200 nM SYTOX Blue (Thermo Fisher) for 30 min at room temperature and rinsed four times with PBS 0.1% Tween-20. Remaining yolk and tails were removed, and the embryos were ventrally mounted in PBS 1.5% low-melt agarose. Primary antibodies were: rabbit anticonnexin-43 (Sigma C6219, 1:50), mouse anti-myosin 4 (Thermo 14-6503-82, 1:250). Secondary antibodies were: goat antirabbit AlexaFluor 633 conjugate (Thermo A-21070) and goat antimouse AlexaFluor 546 conjugate (Thermo A-11003), both applied 1:500.

In situ hybridization was performed with the hybridization chain reaction system (Molecular Instruments), as described by the manufacturer[60]. A custom probe set for *myl7* was designed (Supplementary File 2) for the B1 initiator set, with AlexaFluor594-conjugated amplifier oligonucleotides.

Statistics and reproducibility

Plots were generated in Matplotlib. All boxplots represent IQR with whiskers representing 1.5× IQR. All numbers of independent repeats of experiments are shown alongside *n* values indicating the total number of individual animals. Sample size was determined by the technical demands of the experiments. Individual embryos are not distinguishable at the one-cell stage, and hence were randomly allocated into groups for injection. Sex of animals is not determined at the developmental stage of interest. The researchers were not blinded in this study.

Central tendencies in text are indicated as mean ± s.d. or median (IQR) unless stated otherwise. Statistical analysis was performed using the statannotations and scipy Python packages. The Shapiro–Wilk test for normality was performed on all datasets used for statistical comparisons ($P > 0.05$ for normally distributed data). For paired datasets, a two-tailed paired *t*-test was performed on normally distributed data, whereas a Wilcoxon signed-rank test was performed on non-normally distributed data. For unpaired datasets, a two-tailed unpaired *t*-test was performed on normally distributed data, whereas a Mann–Whitney–Wilcoxon test was performed on non-normally distributed data. Fitting of frequency and ISI coefficient of variation to simulations was performed with a joint mean-squared error approach (Supplementary Information).

Reporting summary

Further information on research design is available in the Nature Portfolio Reporting Summary linked to this article.

Data availability

Raw images are available upon request to the corresponding authors. Source data are provided with this paper.

Code availability

Code is available at https://github.com/adamcohenlab/Jia2023First-Heartbeat.

54. Moro, E. et al. In vivo Wnt signaling tracing through a transgenic biosensor fish reveals novel activity domains. *Dev. Biol.* **366**, 327–340 (2012).
55. Langenbacher, A. D. et al. Mutation in sodium–calcium exchanger 1 (NCX1) causes cardiac fibrillation in zebrafish. *Proc. Natl Acad. Sci. USA* **102**, 17699–17704 (2005).
56. Xiong, F. et al. Specified neural progenitors sort to form sharp domains after noisy Shh signaling. *Cell* **153**, 550–561 (2013).
57. Swinburne, I. A., Mosaliganti, K. R., Green, A. A. & Megason, S. G. Improved long-term imaging of embryos with genetically encoded α-bungarotoxin. *PLoS ONE* **10**, e0134005 (2015).
58. Fan, L. Z. et al. All-optical electrophysiology reveals the role of lateral inhibition in sensory processing in Cortical Layer 1. *Cell* **180**, 521–535.e18 (2020).
59. Witzel, H. R. et al. The LIM protein Ajuba restricts the second heart field progenitor pool by regulating Isl1 activity. *Dev. Cell* **23**, 58–70 (2012).
60. Choi, H. M. T. et al. Third-generation in situ hybridization chain reaction: multiplexed, quantitative, sensitive, versatile, robust. *Development* **145**, dev165753 (2018).

Acknowledgements This work was supported by the Howard Hughes Medical Institute (A.E.C.), a Vannevar Bush Faculty Fellowship (A.E.C.) and the Harvard Medical School John S. Ladue Fellowship in cardiovascular medicine (B.Z.J.). We thank C. E. Burns and C. G. Burns for providing TgBAC(*–36Nkx2.5:ZsYellow*) transgenic fish; N. Chi for providing Tg(*7xTCF-Xla.Siam:nlsmCherry*); I. C. Scott for providing the zACNE20 enhancer element; Y. Shen and R. A. Campbell for providing FR-GECO1c plasmid; L. D. Lavis for providing JaneliaFluor 608 dye; H. C. Davis and F. P. Brooks for developing microscope control software; J. Miller-Henderson, K. Hurley and A. R. Murphy for fish husbandry; and members of the Megason laboratory for assistance with fish husbandry.

Author contributions A.E.C., B.Z.J. and S.G.M. conceived the project and designed experiments. B.Z.J. performed all experiments, data analysis and numerical modelling. B.Z.J. constructed molecular tools and transgenic fish lines. Y.Q., J.D.W.-C. and B.Z.J. performed optical engineering of microscopes. B.Z.J., A.E.C. and S.G.M. wrote the manuscript with input from all authors. A.E.C. and S.G.M. supervised the project.

Competing interests The authors declare no competing interests.

Additional information

Supplementary information The online version contains supplementary material available at https://doi.org/10.1038/s41586-023-06561-z.

Correspondence and requests for materials should be addressed to Sean G. Megason or Adam E. Cohen.

Peer review information *Nature* thanks Emilia Entcheva, Leon Glass and the other, anonymous, reviewer(s) for their contribution to the peer review of this work. Peer reviewer reports are available.

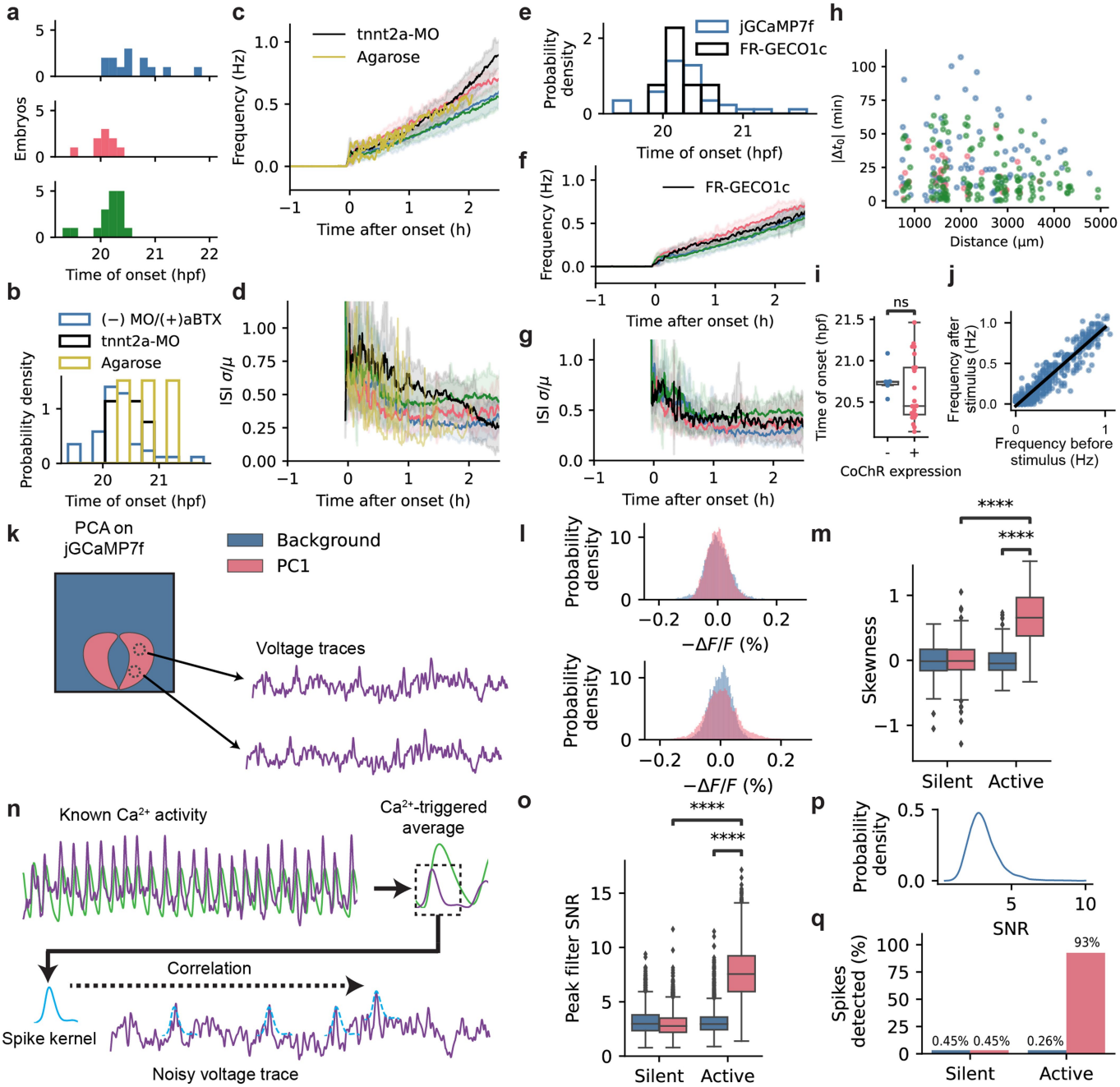

Extended Data Fig. 1 | See next page for caption.

Extended Data Fig. 1 | Validations of experimental approaches. **a**, Histograms of onset time for experimental replicates. **b**, Comparison of time of onset for alpha-bungarotoxin (aBTX) mRNA-injected embryos ($n = 40$), tnnt2a morphants ($n = 12$), and agarose-encased embryos ($n = 3$) respectively. **c**, **d**, Comparison of frequency (**c**) and inter-spike interval coefficient of variation (ISI CV, **d**) as a function of time after the first beat. aBTX mRNA-injected replicates colored corresponding to (**a**). **e**, Time of onset for jGCaMP7f-expressing embryos ($n = 40$) and FR-GECO1c-expressing embryos ($n = 6$). **f**, **g**, Comparison of frequency (**f**) and ISI CV (**g**) for jGCaMP7f and FR-GECO1c-expressing embryos. **h**, Difference in time of onset as a function of distance between all pairwise combinations of embryos in the experiments in (**a**). There was negligible correlation ($r = 0.04, -0.05, -0.18$ for each replicate, respectively), confirming absence of chemical or mechanical coupling between embryos. **i**, Time of onset for embryos +/− CoChR expression and exposed to pulsed blue light for the optogenetic stimulus program in Fig. 4. **j**, Spontaneous beat rate was unchanged before vs. after optogenetic stimulation protocol. **k**, Method of extracting voltage signals from *Tg(z20m:Voltron1-P2A-jGCaMP7f)* heart primordia. **l**, Probability distributions of Voltron1 -ΔF/F in background (blue) and jGCaMP7f principal component 1 (PC1, red) regions, before (top) and after (bottom) initiation of calcium transients. **m**, Skewness of Voltron1 -ΔF/F distribution before (silent) and after (active) initiation of calcium transients. Positive skewness indicates presence of upwards spikes. **n**, Pipeline for performing matched filter analysis (Methods). **o**, Peak matched filter signal-to-noise ratio. **p**, Gaussian kernel density estimate of candidate spike SNR distribution for background regions. **q**, Fraction of candidate spike events with SNR greater than the 95th percentile of **p**. Candidate spike events were identified by performing peak detection on the jGCaMP7f recordings. **a** – **h**, Three replicates of jGCaMP7f and aBTX mRNA-injected embryos at $n = 13$, $n = 9$, $n = 18$ animals respectively, tnnt2a morpholino at $n = 12$ animals, agarose-encased embryos at $n = 3$ animals, 1 experiment. FR-GECO1c and aBTX mRNA-injected embryos at $n = 6$ animals. **i** – **j**, $n = 6$ control animals and $n = 21$ CoChR-expressing animals over 2 experiments. **k**–**q**, 18 recordings with calcium transients detectable by peak finding ("Active"), 22 recordings without ("Silent"), across 36 embryos in one experiment. **m**, 801 traces of regions of interest (ROIs). **o**, 10408 spiking events from ROIs. **q**, 597 putative spikes analyzed (377 in "active" recordings, 220 in "silent" recordings). Boxplots represent interquartile range (IQR; 25th, 50th, 75th percentile) with whiskers representing 1.5×IQR. Statistical test values: (**i**) $p = 0.26$, Mann–Whitney-Wilcoxon two-sided test; (**j**) linear regression $y = 0.97x - 0.024$, $r = 0.953$, $p = 6.6\text{e-}281$, Wald Test; (**m**), active background vs. active PC1 $p = 2.1\text{e-}6$, silent PC1 vs active PC1 $p = 1.4\text{e-}17$, Mann-Whitney-Wilcoxon two-sided test with Benjamini-Hochberg correction. (**o**), $p < 5\text{e-}324$ (below 64-bit numerical precision) in all comparisons shown, Mann-Whitney-Wilcoxon two-sided test with Benjamini-Hochberg correction.

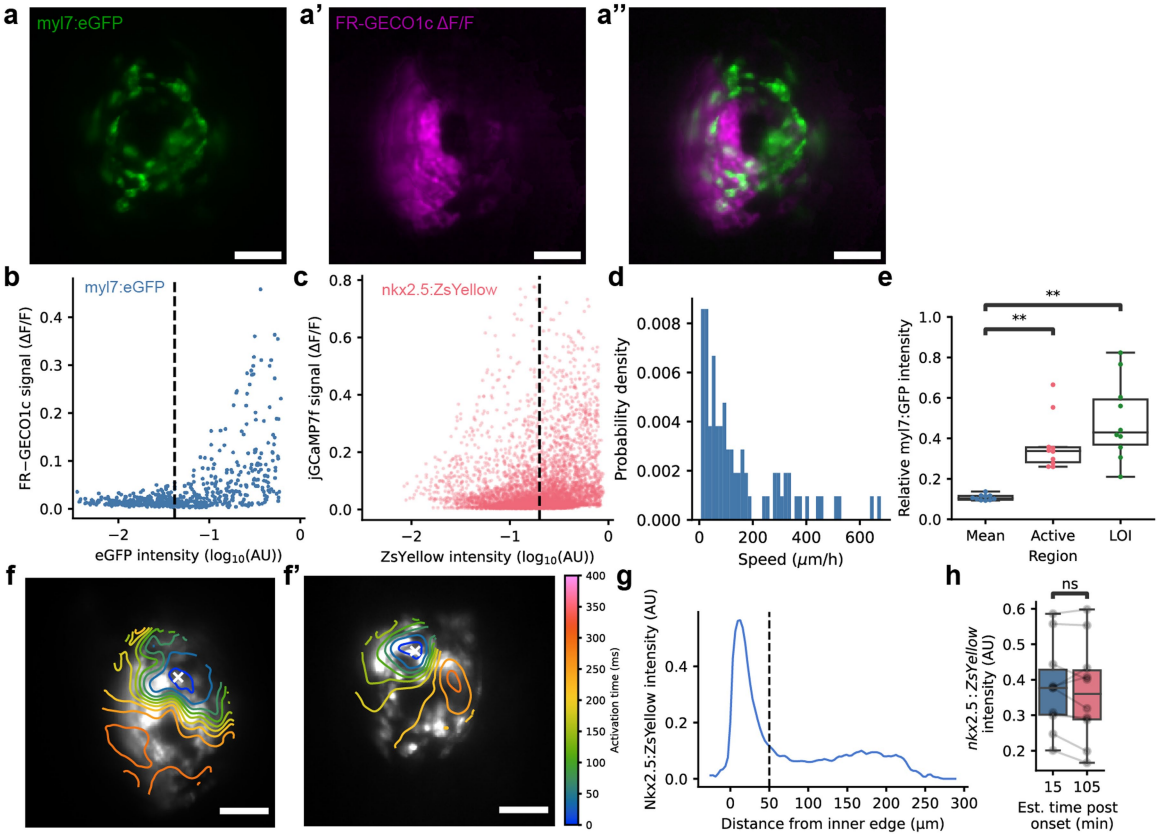

Extended Data Fig. 2 | Calcium dynamics colocalize with genetic markers of developing cardiomyocytes. a, Tg(*myl7:eGFP*) expression in a 20 – 21 hpf embryo. **a'**, Peak ΔF/F of ubiquitously expressed FR-GECO1c during a spike-triggered average video (Methods). **a''**, Merge. Scale bars 50 µm. **b**, Relationship between peak FR-GECO1c ΔF/F and *myl7:eGFP* intensity for tiled regions of interest (Methods). **c**, Relationship between peak jGCaMP7f ΔF/F and *nkx2.5:ZsYellow* intensity for tiled regions of interest. Same embryos as in Fig. 5a–d. **b**, **c**, dashed line indicates 50th percentile of fluorophor intensity. **d**, Distribution of LOI motion speed. **e**, Relative GFP intensity in Ca^{2+} active regions and LOIs, compared to image mean. $n = 10$ embryos, 15 – 45 min post onset. **f** – **f'**, Example activation maps of ubiquitously expressed FR-GECO1c in Tg(*myl7:eGFP*) embryos. GFP in grayscale. Scale bars 50 µm. **g**, Relative *nkx2.5:ZsYellow* intensity as a function of distance from the inner edge of the heart cone. A region approximately <50 µm from the inner edge had stronger expression than more distal cells. **h**, Relative nkx2.5:ZsYellow intensity at the location of the 15 mpo LOI did not change between 15 mpo and 105 mpo, suggesting stable nkx2.5 expression in this region. **a**, **b**, **e**, **f**, $n = 10$ embryos over one experiment, 15 – 45 min post onset. **c**, **h**, Data from Fig. 5a–d ($n = 12$ embryos, 3 experiments). **g**, Data from Extended Data Fig. 4e, f. Boxplots represent interquartile range (IQR; 25th, 50th, 75th percentile) with whiskers representing 1.5×IQR. Statistical test values: (**e**) mean vs. active, $p = 1.953e\text{-}3$, **, mean vs. LOI, $p = 1.953e\text{-}3$, **; (**h**), $p = 0.32$. Two-sided Wilcoxon signed-rank test with Benjamini-Hochberg correction.

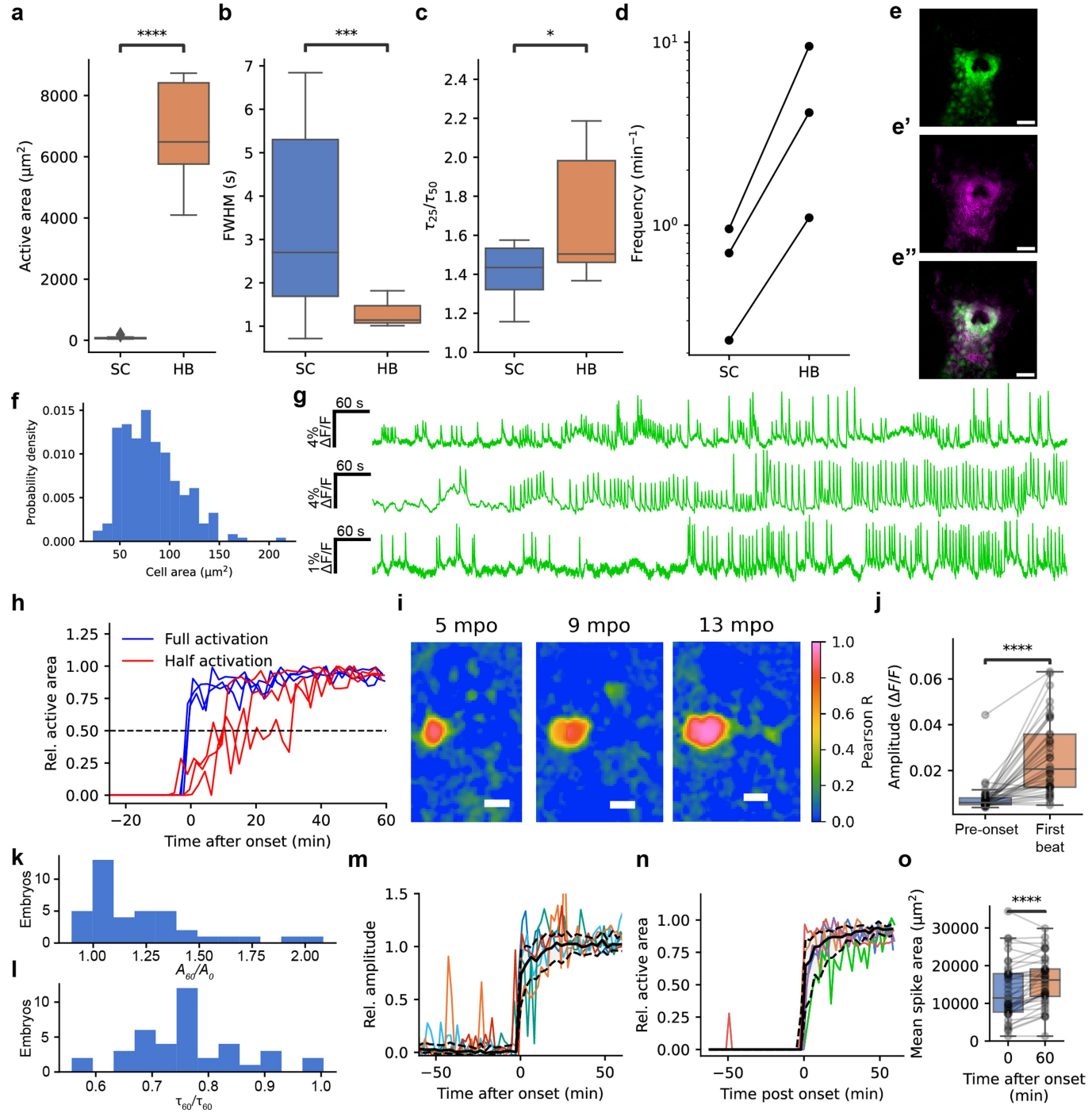

Extended Data Fig. 3 | See next page for caption.

Extended Data Fig. 3 | Spatiotemporal structure of the transition from silent to beating. a, Active area of single-cell (SC) transients (74 ± 32 μm^2) was much lower than that of the first heartbeats (HB, 7000 ± 1400 μm^2). **b**, Single-cell transients were longer lived (3.4 ± 2.1 s) than the first heartbeats (1.3 ± 0.2 s). FWHM: full-width half-maximum. **c**, Single-cell transients had a longer plateau phase than the first heartbeats, as quantified by the ratio of peak width at 25% (τ_{25}) and 50% (τ_{50}) of maximum height. **d**, Single-cell transients were rare (0.2 – 0.7 per minute) compared to the first heartbeats (1 – 9.5 per minute). **a** – **d**, Data from 19 single-cell transients and 50 beats across n = 3 embryos over 3 experiments. **e** – **e''**, Maximum intensity projection fluorescence images of 21-somite stage Tg(*-36nkx2.5:ZsYellow;zACNE20:2xLyn-mCherry*) heart cone (5/5 embryos over 1 experiment). **e**, *nkx2.5:ZsYellow*. **e'**, *zACNE20:2xLyn-mCherry*. **e''**, Merge. **f**, Cell area distribution. Mean area 82 μm^2 (± 29 μm^2 SD). n = 5 embryos, 254 cells, over 1 experiment. Scale bars 50 μm. Mean ± SD for all values in caption. **g**, jGCaMP7f fluorescence starting from 2 min after the first heartbeat in embryos with spontaneous initiation in half the heart. The traces were averaged over the whole heart, so traces that engaged half the heart had approximately half the apparent amplitude of traces that engaged the whole heart. **h**, Relative active areas of the traces in (**g**) compared to representative traces of embryos with full-tissue initiation. Area was averaged in a 2-minute sliding window. **i**, Pearson correlation between fluorescence dynamics of individual pixels and the mean segmented heartbeat jGCaMP7f activity at different timepoints. The sharp boundary in the 9 min post onset (mpo) image is due to roughly half the heart being engaged in some but not all beats. Same experiments as in Fig. 1. Scale bars 100 μm. **j**, Amplitude of the first detected calcium transient compared to maximum fluctuation from mean in the previous 2 min. **k**, Ratio of calcium transient amplitudes (ΔF/F) 60 min post onset (mpo, A_{60}) and 0 mpo (A_0). **l**, Ratio of transient widths (full-width half-maximum) 60 min mpo (τ_{60}) and 0 mpo (τ_0). **m**, Amplitude of calcium transients as a function of time, aligned relative to first beat and normalized relative to initial beats. **n**, Active area of calcium transients as a function of time, aligned relative to first beat and normalized relative to initial beats (Methods). **m**,**n**, Colored lines show representative single-embryo traces. Black line shows median. Shading and dashed lines show interquartile range. **o**, Calcium spike area increased from 13490 ± 7730 μm^2 at 0 mpo to 15840 ± 6400 μm^2 at 60 mpo. **j** – **o**, n = 39 embryos across 3 experiments, same individuals as Figs. 1–2. Boxplots represent interquartile range (IQR; 25th, 50th, 75th percentile) with whiskers representing 1.5×IQR. Statistical test values: (**a**) Two-sided Mann-Whitney-Wilcoxon test, p = 6.5e-11, ****; (**b**) Two-sided Mann-Whitney-Wilcoxon test, p = 1.3e-4, ***; (**c**) Two-sided Mann-Whitney-Wilcoxon test, p = 0.015, *; (**j**) Two-sided Wilcoxon signed-rank test, p = 1.23e-7, ****; (**o**) Two-sided paired t-test, p = 5.4e-5, ****.

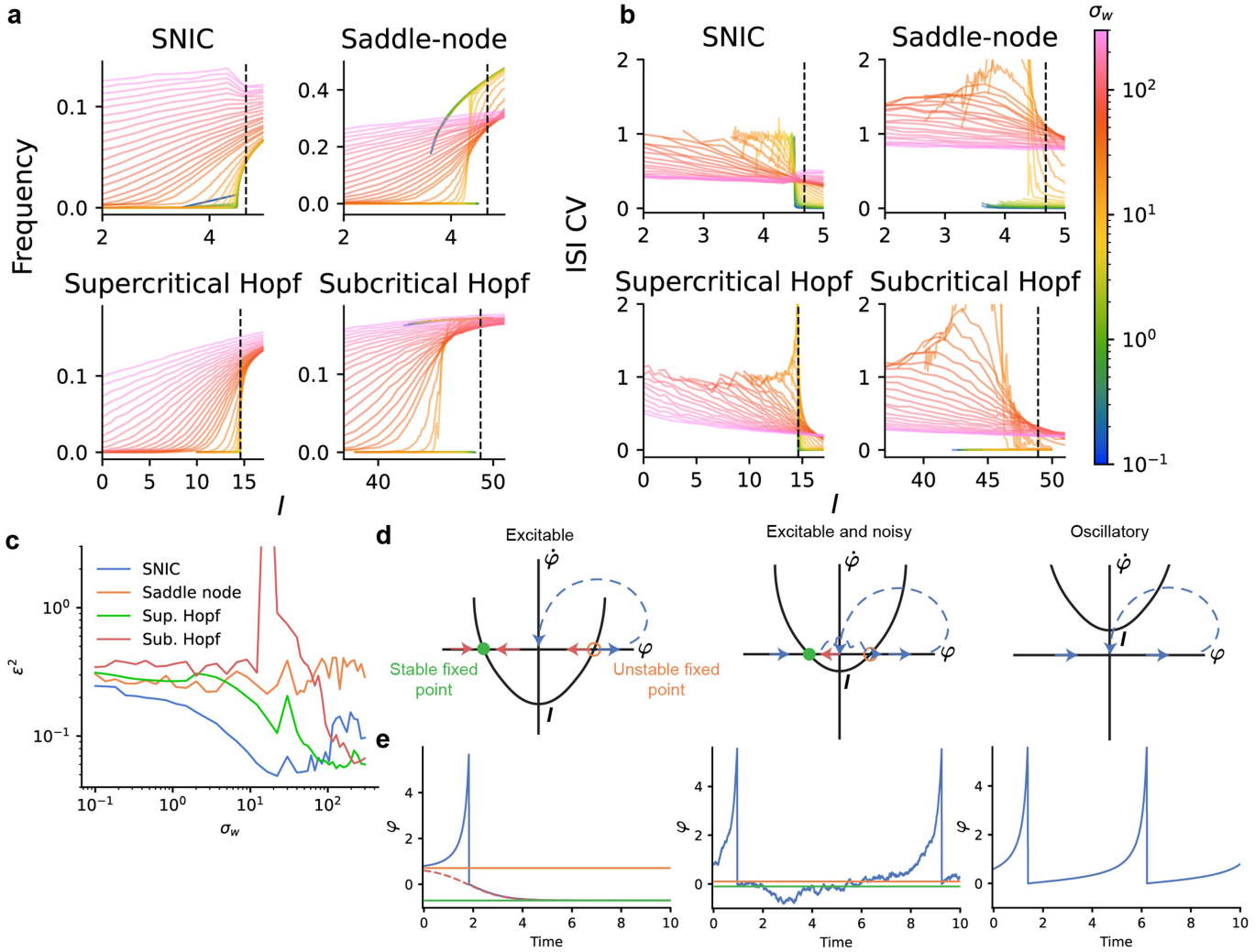

Extended Data Fig. 4 | Classification of the bifurcation from silent to beating. a, Mean frequency and **b**, inter-spike interval (ISI) coefficient of variation (CV) in simulated Morris-Lecar oscillators as a function of input current *I* and noise σ_w. Parameters given in Supplementary Table 2, were selected to drive each of the four types of co-dimension 1 bifurcation. **c**, Squared error (Supplementary Text) of experimental fits to each bifurcation at different values of σ_w. **d**, Spiking regimes across the SNIC bifurcation of the noisy quadratic integrate-and-fire (QIF) model (Supplementary Information Equation 2), shown by $\dot{\varphi}$ as a function of φ. **e**, Simulated example traces for each spiking regime.

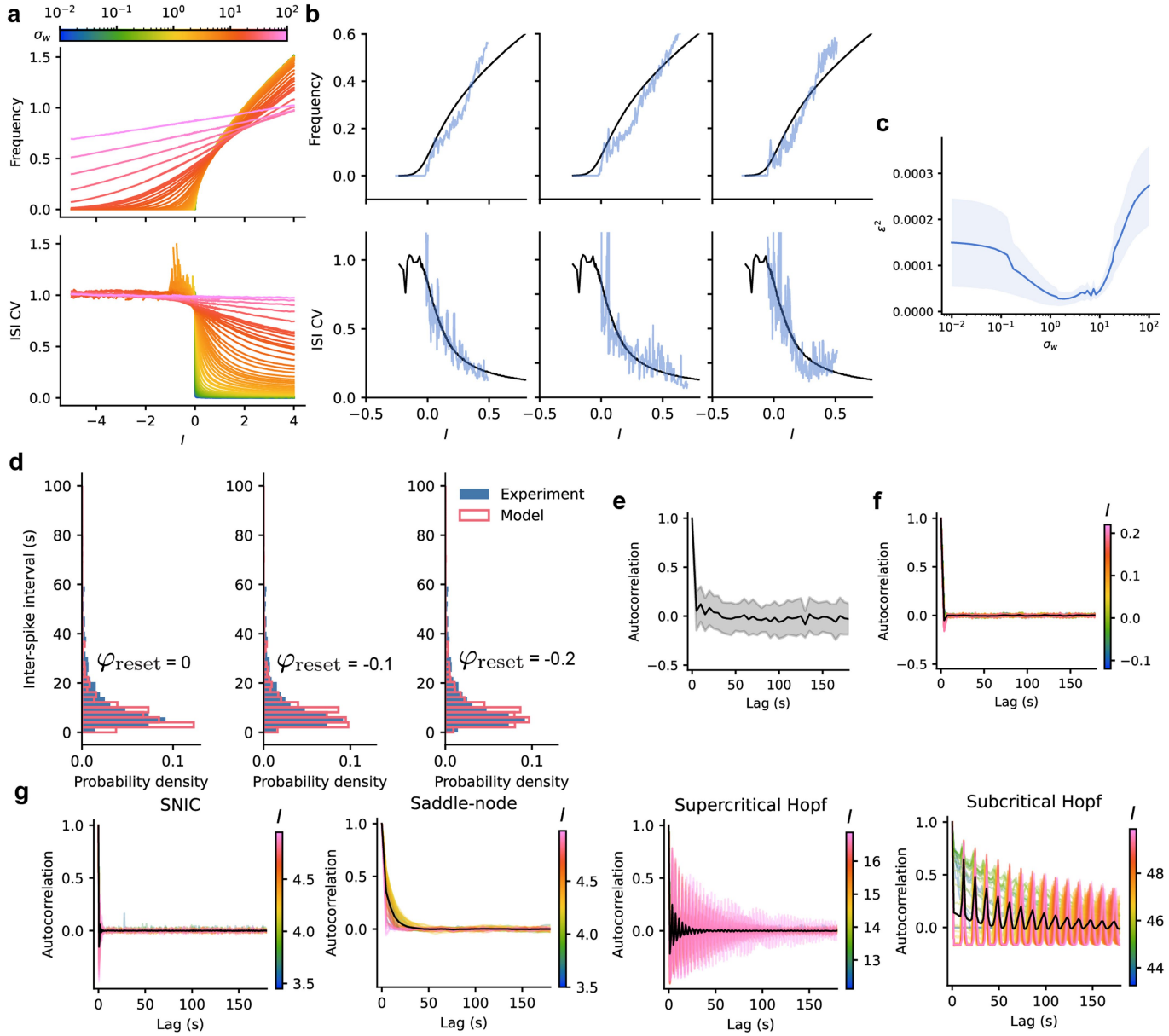

Extended Data Fig. 5 | A noisy quadratic integrate-and-fire model captures the statistics of the first heartbeats. a, Simulated frequency and ISI CV for different values of noise σ_w. **b**, Example fits (top: frequency, bottom: ISI CV) of individual embryo data (blue) to simulation (black) with choices of σ_w which minimized squared error. **c**, Mean squared error of fits of simulated spike statistics to data as a function of σ_w ($n = 39$ embryos). **d**, Histograms of experimental and QIF-generated ISIs for the first 20 heartbeats, using different φ_{reset} values. Decreasing φ_{reset} modelled an increasing refractory period, and corrected the overrepresentation of short ISIs in the model relative to the data. **e**, Experimental autocorrelation of instantaneous frequency averaged over the first 50 heartbeats. **f**, Autocorrelation of instantaneous frequency in the QIF model with experimentally fitted σ_w and varying values of I. **g**, Autocorrelation of instantaneous frequency in the four bifurcation classes of the Morris-Lecar model, calculated using experimentally fitted σ_w and varying values of I.

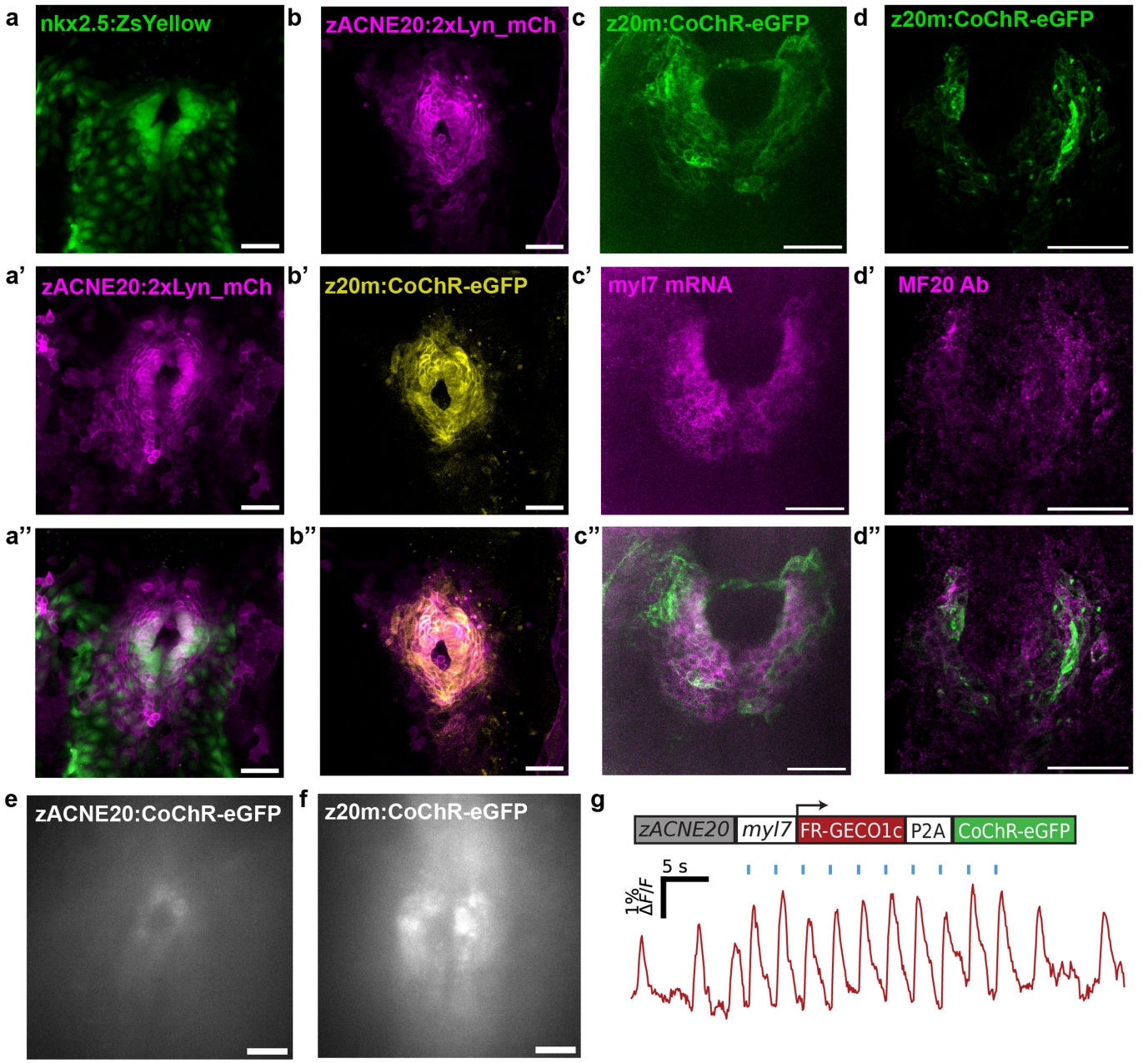

Extended Data Fig. 6 | Expression patterns of *zACNE20* and *zACNE20-myl7 (z20m)* promoters in the early heart. a–a”, Heart primordium in a 20-somite stage (ss) Tg(-36*nkx2.5:ZsYellow;zACNE20:2xLyn_mCherry*) embryo (5/5 embryos). **b–b”**, Heart cone in a 22 ss stage Tg(*zACNE20:2xLyn_mCherry; zACNE20-myl7:FRGECO1c-P2A-CoChR-eGFP*) embryo (6/6 embryos). **c–c”**, Heart primordium in an 18 – 19ss *Tg(z20m:FRGECO1c-P2A-CoChR-eGFP)* embryo stained for *myl7* using HCR-FISH (9/9 embryos). **d–d”**, Heart primordium in an 16 – 18ss *Tg(z20m:FRGECO1c-P2A-CoChR-eGFP)* embryo immunostained using MF20 antibody (6/6 embryos over 3 experiments). **a – d**, All images are confocal maximum intensity projections. **e**, **f**, *z20m* produces stronger expression than *zACNE20* at the same stage. Widefield images at 20-21 ss. **g**, example calcium recording and optogenetic stimulus in *zACNE20-myl7: FRGECO1c-P2A-CoChR-eGFP* at ~21 – 22 hpf (without additional mRNA). All scale bars 50 µm.

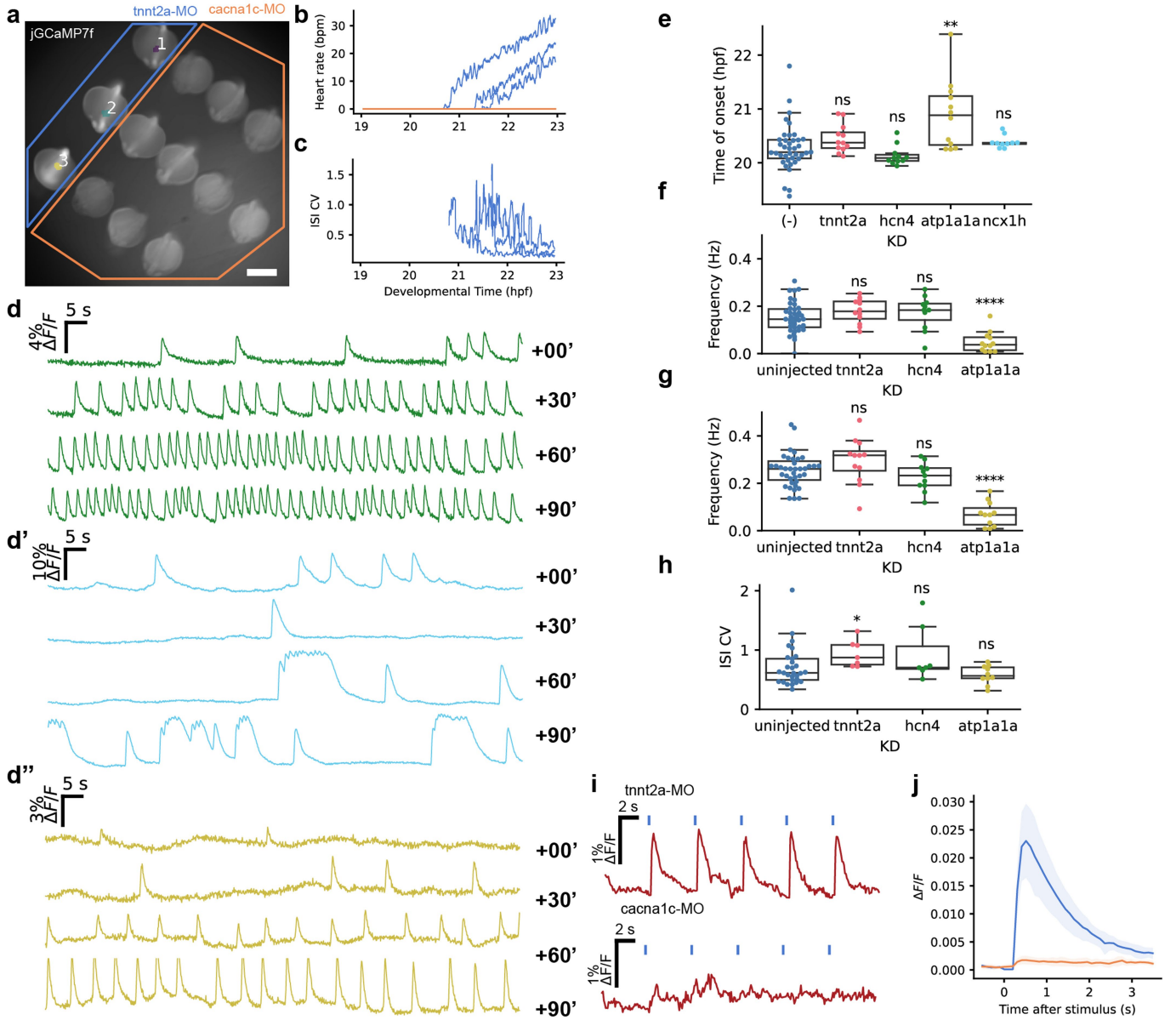

Extended Data Fig. 7 | Roles of pacemaker ion transporters in initiation of spontaneity and excitability. a, Automatic segmentation (Methods) located heartbeats in control embryos but not in embryos injected with the *cacna1c* morpholino. *tnnt2a* KD, $n = 3$ embryos; *cacna1c* KD, $n = 10$ embryos. All embryos were injected with jGCaMP7f mRNA. Scale bar 500 µm. **b**, **c**, The heartbeats became faster and more regular after initiation in *tnnt2a*-MO embryos. Manually selected ROIs in the *cacna1c* morphants did not show spontaneous activity. **d** – **d''**, Traces of jGCaMP7f fluorescence at 0, 30, 60, and 90 min after onset for embryos injected with morpholinos for **d** *hcn4*, **d'** *ncx1h*, **d''** *atp1a1a* (Na^+,K^+-ATPase α-subunit). **e**, Time of onset for morphants. **f**, Mean frequency at 30 min post onset. **g**, Mean frequency at 60 min post onset. **h**, Inter-spike interval coefficient of variation (ISI CV) at a mean frequency of 0.1 Hz. *ncx1h* morphants were omitted in **c** – **e** because the plateaus prevented unambiguous determination of spike times. **e** – **h**, Uninjected, $n = 39$ embryos; *tnnt2a* KD, $n = 12$ embryos; *hcn4* KD, $n = 11$ embryos; *ncx1h* KD, $n = 10$ embryos; *atp1a1a* KD, $n = 12$ embryos. Uninjected samples collected over 3 experiments, other samples collected over 1 experiment each. **e** – **h**, Boxplots represent interquartile range (IQR; 25th, 50th, 75th percentile) with whiskers representing 1.5×IQR. **i**, Example traces of FR-GECO1c dynamics (red) with pulsed CoChR stimulus (blue) directed to the entire heart of individual embryos. **j**, Stimulus-triggered average of calcium activity in control (blue) and *cacna1c* morphants (orange, population mean ± SD). **i**, **j**, *tnnt2a* KD, $n = 11$ embryos, *cacna1c* KD, $n = 14$ embryos. All recordings acquired at 10 Hz. All embryos were *zACNE20-myl7:FRGECO1c-P2A-CoChR-eGFP* (+/-) injected with FR-GECO1c mRNA. Statistical test values: **e** – **h**, Mann-Whitney-Wilcoxon two-sided test with Benjamini-Hochberg correction. (**e**) uninjected vs. *tnnt2a*, $p = 0.0775$; uninjected vs. *hcn4*, $p = 0.11$; uninjected vs. *atp1a1a*, $p = 1.23e\text{-}3$; uninjected vs. *ncx1h*, $p = 0.0847$. (**f**) uninjected vs *tnnt2a*, $p = 0.149$; uninjected vs. *hcn4*, $p = 0.228$; uninjected vs. *atp1a1a*, $p = 2.11e\text{-}5$. (**g**) uninjected vs. *tnnt2a*, $p = 0.096$; uninjected vs. *hcn4*, $p = 0.256$; uninjected vs. *atp1a1a*, $p = 7.71e\text{-}7$. (**h**) uninjected vs *tnnt2a*, $p = 0.0158$; uninjected vs. *hcn4*, $p = 0.165$; uninjected vs *atp1a1a*, $p = 0.376$.

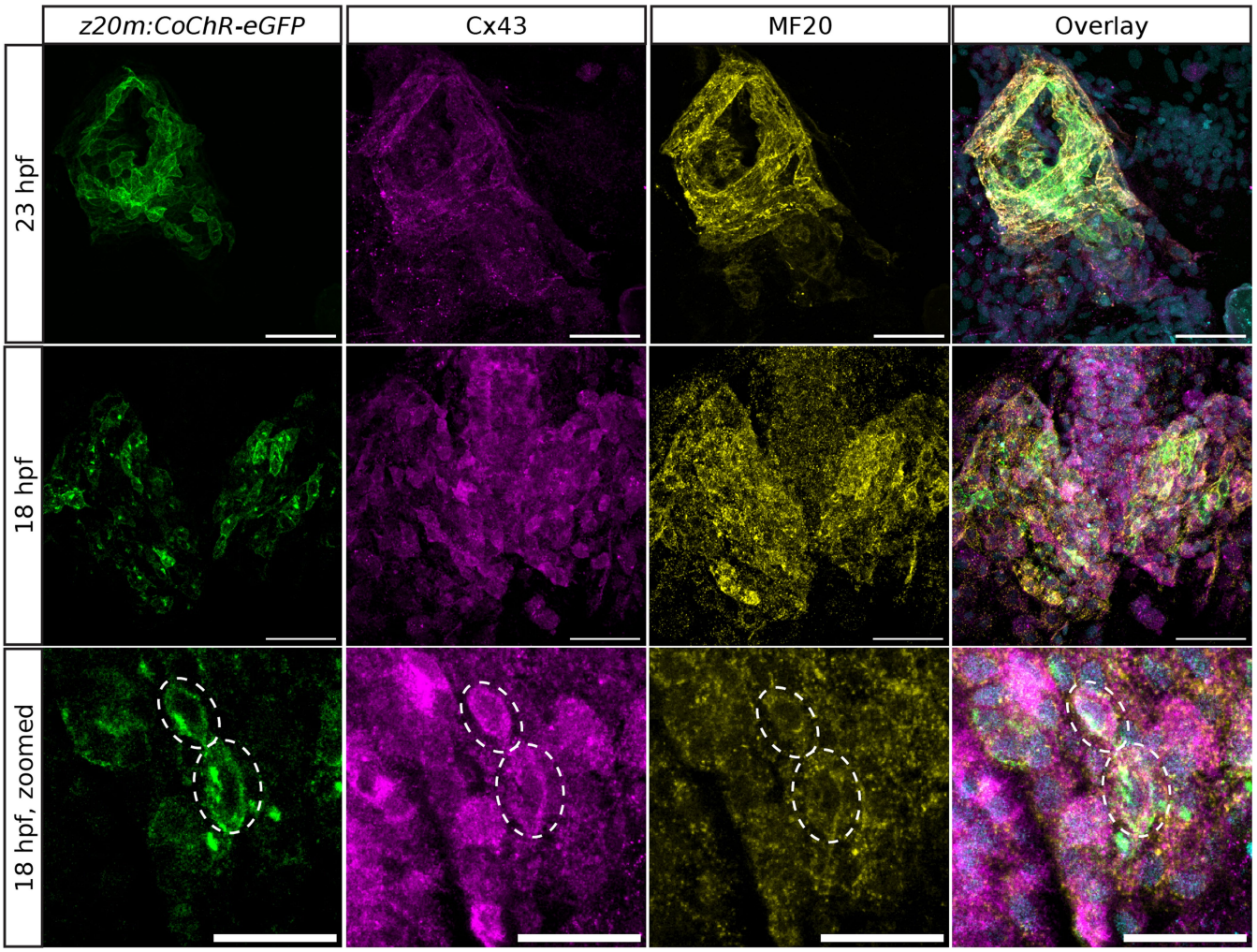

Extended Data Fig. 8 | Connexin-43 is expressed in the cardiac primordium before fusion. *Tg*(*z20m:FRGECO1c-P2A-CoChR-eGFP*) fish were immunostained for connexin-43 and sarcomeric myosin (MF20). Examples of triple-positive cells indicated by dotted circles on the bottom row. Top row: 4/4 embryos over 1 experiment. Middle and bottom rows: 6/6 embryos over 3 experiments (same individuals as Extended Data Fig. 6d). Cyan in overlay: nuclear staining by SYTOX Blue. Scale bars 50 µm (top and middle row), 25 µm (bottom row).

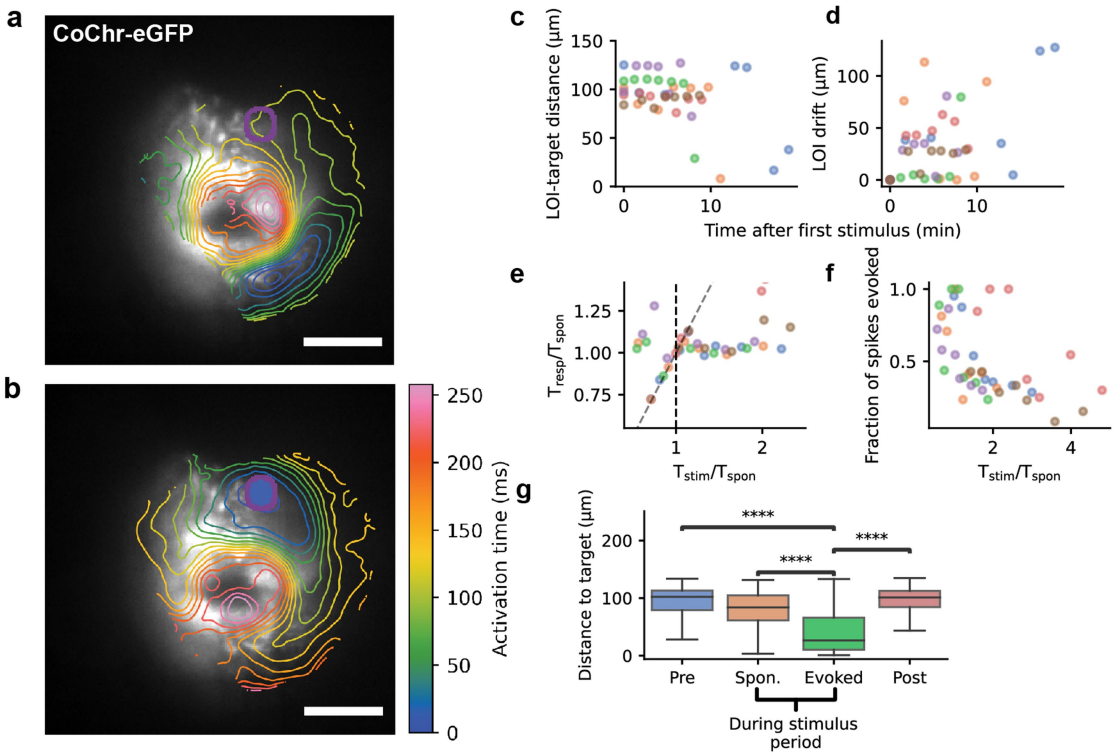

Extended Data Fig. 9 | Optogenetic pacing induces overdrive suppression in the heart cone. a, Activation map of spontaneous activity (spike-triggered average, $n = 9$ spikes) in *Tg(z20m:FRGECO1c-P2A-CoChR-eGFP)* embryo. Purple circle indicates region to be stimulated in (**b**). **b**, Activation map of evoked activity (spike-triggered average, $n = 19$ spikes) in the same heart as (**a**). Scale bars 50 µm. **c**, Distance between spontaneous LOI and fixed "target region" after repeated pacing at different frequencies at the target region. **d**, Drift of the spontaneous LOI from its first recorded position was uncorrelated with repeated pacing. **e**, A target region away from the spontaneous LOI was paced with period T_{stim}. Heartbeat was characterized by T_{spon} = period of spontaneous activity in absence of stimulus, and T_{resp} = period of activity during periodic stimulus. CoChR activation only paced the heart (i.e. $T_{resp}/T_{stim} \approx 1$) when $T_{stim} < T_{spon}$. At the highest stimulus frequencies, the heart showed a period doubling, i.e. $T_{resp}/T_{stim} \approx 2$. **f**, Ratio of number of evoked spikes to number of total spikes (spontaneous + evoked) during the 30-second stimulus period. At a lower pacing interval, evoked spikes comprised a larger fraction of the total. "Evoked spikes" were defined as spikes which occurred within 200 ms of a pulse of blue light. (**c** – **f**) Each color represents one fish. **g**, Distance between the target region and the LOI of each individual spike grouped by timing and whether the spike was evoked. Evoked spikes had LOI significantly closer to target than any other category. Boxplot represents interquartile range (IQR; 25th, 50th, 75th percentile) with whiskers representing 1.5×IQR. (**c** – **g**) Number of beats collected per category – "Pre": 306; "During": 309; "Stim": 363; "Post": 281. $n = 6$ embryos in one experiment. Statistical test values: Pre. vs Evoked, $U = 9.2e4$, $p = 1.1e\text{-}47$, ****; Post vs Evoked, $U = 1.5e4$, $p = 2.3e\text{-}52$, ****; Spon. vs Evoked, $U = 8.6e4$, $p = 2.6e\text{-}33$, ****. Mann-Whitney Wilcoxon two-sided test with Benjamini-Hochberg correction.

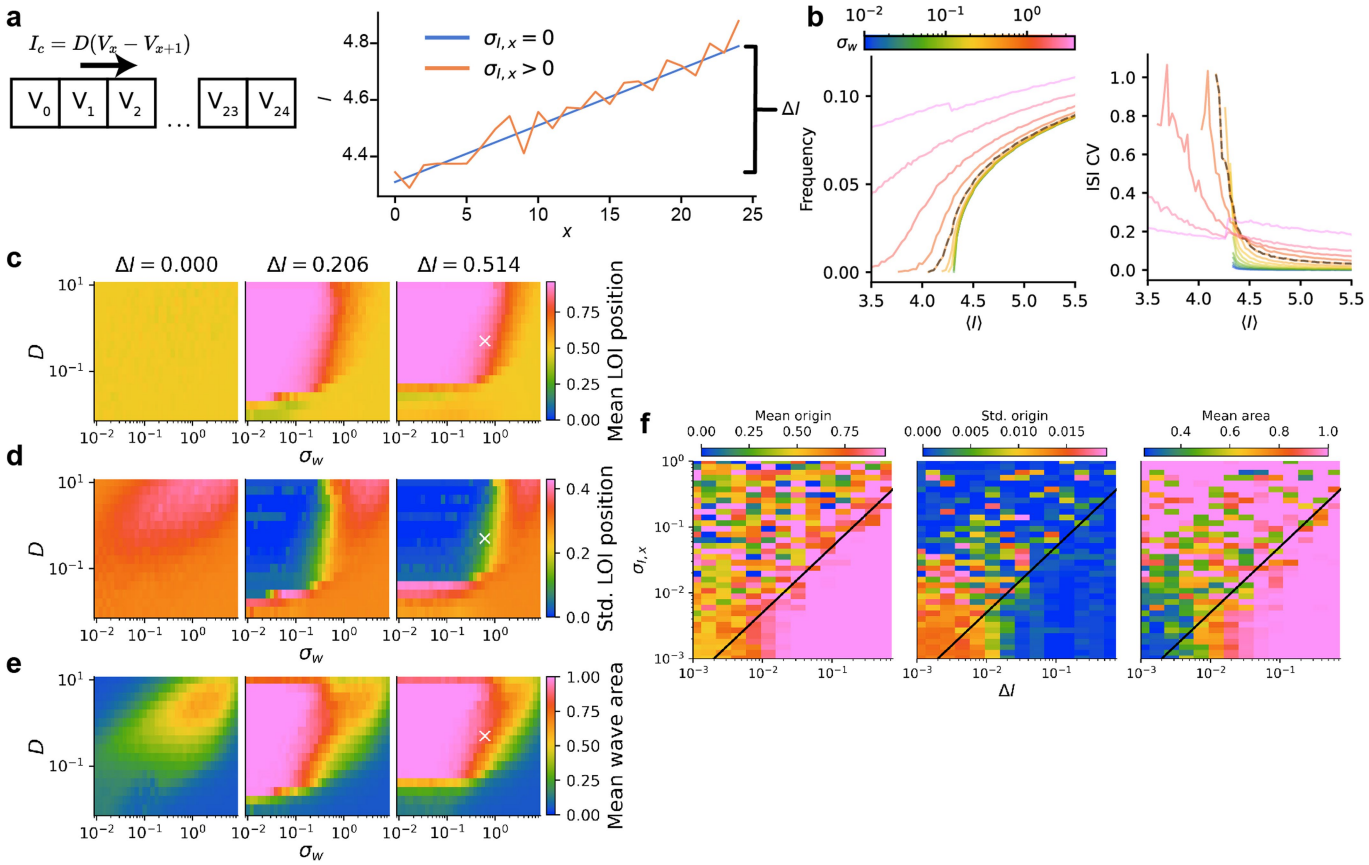

Extended Data Fig. 10 | Robustness of wave geometry in heterogeneous coupled SNIC oscillators. (**a**) Schematic for chain of Morris-Lecar oscillators coupled by a current I_c which depends on coupling strength D (left); and spatial distribution of I for different choices of ΔI and $\sigma_{I,x}$ (right). (**b**) Mean frequency (f) and inter-spike interval coefficient of variation (ISI CV) for a chain of 25 oscillators with $D = 0.5$, and current gradient $\Delta I = 0.514$. Simulation with $\sigma_w = 0.618$ (compare qualitatively to experiments) marked with dashed black lines. **c** – **e**, Simulated wave properties as a function of σ_w and D. Here I attained its highest value at normalized $x = 1.0$. **c**, Normalized mean LOI position. **d**, Standard deviation of LOI position. **e**, Normalized wave area. Parameter choice for dashed line in (**b**) indicated with white "X". **f**, Wave geometry as a function of ΔI and $\sigma_{I,x}$. Black line indicates the line $\sigma_{I,x} = 0.5\,\Delta I$. For sufficiently large ΔI, full-tissue wave propagation occurred with stable LOI at one end of the chain. In high variability, i.e. large $\sigma_{I,x}$, a stable LOI driving full-tissue waves (low position standard deviation, high normalized mean area) can appear at positions that are not the end of the chain. (**e**, **f**) $\langle I \rangle = 4.68$, $\sigma_w = 0.03$.

nature portfolio

Corresponding author(s): Sean Megason, Adam E. Cohen

Last updated by author(s): Aug 9, 2023

Reporting Summary

Nature Portfolio wishes to improve the reproducibility of the work that we publish. This form provides structure for consistency and transparency in reporting. For further information on Nature Portfolio policies, see our Editorial Policies and the Editorial Policy Checklist.

Statistics

For all statistical analyses, confirm that the following items are present in the figure legend, table legend, main text, or Methods section.

n/a	Confirmed	
☐	☒	The exact sample size (*n*) for each experimental group/condition, given as a discrete number and unit of measurement
☐	☒	A statement on whether measurements were taken from distinct samples or whether the same sample was measured repeatedly
☐	☒	The statistical test(s) used AND whether they are one- or two-sided *Only common tests should be described solely by name; describe more complex techniques in the Methods section.*
☐	☒	A description of all covariates tested
☐	☒	A description of any assumptions or corrections, such as tests of normality and adjustment for multiple comparisons
☐	☒	A full description of the statistical parameters including central tendency (e.g. means) or other basic estimates (e.g. regression coefficient) AND variation (e.g. standard deviation) or associated estimates of uncertainty (e.g. confidence intervals)
☐	☒	For null hypothesis testing, the test statistic (e.g. *F*, *t*, *r*) with confidence intervals, effect sizes, degrees of freedom and *P* value noted *Give P values as exact values whenever suitable.*
☒	☐	For Bayesian analysis, information on the choice of priors and Markov chain Monte Carlo settings
☒	☐	For hierarchical and complex designs, identification of the appropriate level for tests and full reporting of outcomes
☐	☒	Estimates of effect sizes (e.g. Cohen's *d*, Pearson's *r*), indicating how they were calculated

Our web collection on statistics for biologists contains articles on many of the points above.

Software and code

Policy information about availability of computer code

Data collection	MATLAB R2022a and National Instruments Labview 2015 control of custom instruments was used to acquire the data, as described in previous literature (He et al. Nat. Meth. 2022; Parot et al. J. Neurosci 2019). Zeiss ZEN 3.2 software was used to collect confocal microscopy data. Autodesk Inventor 2020 was used to design the CAD file for production of custom mount used in our experimental preparation.
Data analysis	MATLAB R2022a, ImageJ (v 1.53t) and open-source Python (v3.9) packages were used to analyze data. Custom Python and MATLAB codes were written and are provided at https://github.com/adamcohenlab/Jia2023FirstHeartbeat. Python package versions are given in "spikecounter/config/environment.yml" in this repository.

For manuscripts utilizing custom algorithms or software that are central to the research but not yet described in published literature, software must be made available to editors and reviewers. We strongly encourage code deposition in a community repository (e.g. GitHub). See the Nature Portfolio guidelines for submitting code & software for further information.

Data

Policy information about availability of data

All manuscripts must include a data availability statement. This statement should provide the following information, where applicable:

- Accession codes, unique identifiers, or web links for publicly available datasets
- A description of any restrictions on data availability
- For clinical datasets or third party data, please ensure that the statement adheres to our policy

All numerical values in figures are included in the Source Data files. Raw video (~5 TB) is archived on the Cohen Lab server and is available upon request.

Human research participants

Policy information about studies involving human research participants and Sex and Gender in Research.

Reporting on sex and gender	not applicable
Population characteristics	not applicable
Recruitment	not applicable
Ethics oversight	not applicable

Note that full information on the approval of the study protocol must also be provided in the manuscript.

Field-specific reporting

Please select the one below that is the best fit for your research. If you are not sure, read the appropriate sections before making your selection.

☒ Life sciences ☐ Behavioural & social sciences ☐ Ecological, evolutionary & environmental sciences

For a reference copy of the document with all sections, see nature.com/documents/nr-reporting-summary-flat.pdf

Life sciences study design

All studies must disclose on these points even when the disclosure is negative.

Sample size	Sample sizes were as large as practical, given the technical demands of the experiments and the requirements to image embryos at specific times post-fertilization. Measures of statistical significance (p-values after multiple hypothesis correction) confirmed that sample sizes were large enough to reject a threshold of Type I error on the population means (p=0.05). For false negatives, post-hoc power analyses are inappropriate (Levine & Ensom Pharmacotherapy 2001). All negative results on statistical tests are presented transparently, with all data points shown. All negative results are either supported by other observations (Fig. 4f by Fig. 3; ED Fig. 1i by ED Fig. 1j, ED Fig. 3h by Fig. 5 and many literature studies), or have associated positive groups with similar sample size, which sets a baseline for biological relevance (ED Fig. 7d-h).
Data exclusions	Data were excluded when there were excessive motion artifacts or low signal-to-noise ratio due to poor expression of the reporter (manually assessed for each experiment).
Replication	All experiments had at least 3 biological replicates, and all replicates gave consistent results. Additionally, most experiments were independently repeated at least twice and were successfully reproduced. Some experiments requested in revision were not repeated (but still included at least three biological replicates). The robustness of our experimental preparation from trial to trial and between different biological conditions is characterized in detail in Extended Data Fig. 1.
Randomization	Experiments with different conditions were performed using eggs collected from a single mating. Embryos were randomly allocated into groups for 1-cell injections; individuals cannot be distinguished at the 1-cell stage.
Blinding	During data collection, blinding was impossible due to the complexity of assigning different optical and genetic conditions to individuals. All analysis was performed automatically and identically over individual samples using software and hence was blinded.

Reporting for specific materials, systems and methods

We require information from authors about some types of materials, experimental systems and methods used in many studies. Here, indicate whether each material, system or method listed is relevant to your study. If you are not sure if a list item applies to your research, read the appropriate section before selecting a response.

Materials & experimental systems

n/a	Involved in the study
☐	☒ Antibodies
☒	☐ Eukaryotic cell lines
☒	☐ Palaeontology and archaeology
☐	☒ Animals and other organisms
☒	☐ Clinical data
☒	☐ Dual use research of concern

Methods

n/a	Involved in the study
☒	☐ ChIP-seq
☒	☐ Flow cytometry
☒	☐ MRI-based neuroimaging

Antibodies

Antibodies used

Primary antibodies were: rabbit anti-connexin-43 (Sigma C6219), mouse anti-myosin 4 (Thermo 14-6503-82). Secondary antibodies were goat anti-rabbit AlexaFluor 633 conjugate (Thermo A-21070) and goat anti-mouse AlexaFluor 546 conjugate (Thermo A-11003). Dilutions are provided in Methods section.

Validation

Sigma C6219 (anti-Cx43):

Rattka, M., Westphal, S., Gahr, B.M., Just, S., Rottbauer, W. (2021) Spen deficiency interferes with Connexin 43 expression and leads to heart failure in zebrafish. Journal of Molecular and Cellular Cardiology. 155:25-35.
-Western Blot (Fig. 4)

Chi, N.C., Shaw, R.M., Jungblut, B., Huisken, J., Ferrer, T., Arnaout, R., Scott, I., Beis, D., Xiao, T., Baier, H., Jan, L.Y., Tristani-Firouzi, M., and Stainier, D.Y. (2008) Genetic and Physiologic Dissection of the Vertebrate Cardiac Conduction System. PLoS Biology. 6(5):e109.
-IF (Fig. 5)

Musso, G., Tasan, M., Mosimann, C., Beaver, J.E., Plovie, E., Carr, L.A., Chua, H.N., Dunham, J., Zuberi, K., Rodriguez, H., Morris, Q., Zon, L., Roth, F.P., and MacRae, C.A. (2014) Novel cardiovascular gene functions revealed via systematic phenotype prediction in zebrafish. Development (Cambridge, England). 141(1):224-235.
-IF (Fig. 5)

Panáková, D., Werdich, A. & MacRae, C. Wnt11 patterns a myocardial electrical gradient through regulation of the L-type Ca2+ channel. Nature 466, 874–878 (2010).
-IF (Fig. 1, Fig. 4)

Thermo 14-6503-82 (anti-myosin 4):

Juan, T., Ribeiro da Silva, A., Cardoso, B. et al. Multiple pkd and piezo gene family members are required for atrioventricular valve formation. Nat Commun 14, 214 (2023).
-IF (Fig 1-3, 5,6)

Boezio, G.L.M., Zhao, S., Gollin, J., Priya, R., Mansingh, S., Guenther, S., Fukuda, N., Gunawan, F., Stainier, D.Y.R. (2022) The developing epicardium regulates cardiac chamber morphogenesis by promoting cardiomyocyte growth. Disease models & mechanisms. 16(5).
-IF (Fig. S6)

Pham, Duc H., Charles R. Dai, Belle Y. Lin, and Jonathan T. Butcher. "Local fluid shear stress operates a molecular switch to drive fetal semilunar valve extension." Developmental Dynamics 251, no. 3 (2022): 481-497.
-IF (Figs. 1, 3, 4, 10).

Animals and other research organisms

Policy information about studies involving animals; ARRIVE guidelines recommended for reporting animal research, and Sex and Gender in Research

Laboratory animals	Zebrafish Danio rerio, AB strain, 3 months - 2 years old were used for breeding. Experiments were performed on embryos 0 - 24 h post-fertilization.
Wild animals	No wild animals were used in the study.
Reporting on sex	Male and female adults were matched for mating. At the developmental stage when experiments were conducted, sex has not yet been determined.
Field-collected samples	No field collected samples were used in the study.
Ethics oversight	Institutional Animal Care and Use Committee of Harvard University, Harvard Medical Area Standing Committee on Animals

Note that full information on the approval of the study protocol must also be provided in the manuscript.